Systems/Circuits

Pathways for Memory, Cognition and Emotional Context: Hippocampal, Subgenual Area 25, and Amygdalar Axons Show Unique Interactions in the Primate Thalamic Reuniens Nucleus

Mary Kate P. Joyce,[1,6,*] Laura G. Marshall,[1,2,*] Shimrani L. Banik,[1] Jingyi Wang,[1,3] Danqing Xiao,[1,4] Jamie G. Bunce,[5] and Helen Barbas[1,2]

[1]Neural Systems Laboratory, Department of Health Sciences, Boston University, Boston, Massachusetts 02215, [2]Graduate Program in Neuroscience, School of Medicine, Boston University, Boston, Massachusetts 02215, [3]Department of Psychological and Brain Sciences, University of California, Santa Barbara, California 93106, [4]STEM Department, Regis College, Weston, Massachusetts 02493, [5]Department of Biology, Northeastern University, Boston, Massachusetts 02115, and [6]Department of Neuroscience, Yale School of Medicine, New Haven, Connecticut 06510

The reuniens nucleus (RE) is situated at the most ventral position of the midline thalamus. In rats and mice RE is distinguished by bidirectional connections with the hippocampus and medial prefrontal cortex (mPFC) and a role in memory and cognition. In primates, many foundational questions pertaining to RE remain unresolved. We addressed these issues by investigating the composition of the rhesus monkey RE in both sexes by labeling for GABA, a marker of inhibitory neurons, and for the calcium-binding proteins parvalbumin (PV), calbindin (CB), and calretinin (CR), which label thalamic excitatory neurons that project to cortex. As in rats and mice, the macaque RE was mostly populated by CB and CR neurons, characteristic of matrix-dominant nuclei, and had bidirectional connections with hippocampus and mPFC area 25 (A25). Unlike rodents, we found GABAergic neurons in the monkey RE and a sparser but consistent population of core-associated thalamocortical PV neurons. RE had stronger connections with the basal amygdalar complex than in rats or mice. Amygdalar terminations were enriched with mitochondria and frequently formed successive synapses with the same postsynaptic structures, suggesting an active and robust pathway to RE. Significantly, hippocampal pathways formed multisynaptic complexes that uniquely involved excitatory projection neurons and dendrites of local inhibitory neurons in RE, extending this synaptic principle beyond sensory to high-order thalamic nuclei. Convergent pathways from hippocampus, A25, and amygdala in RE position it to flexibly coordinate activity for memory, cognition, and emotional context, which are disrupted in several psychiatric and neurologic diseases in humans.

Key words: **consciousness; core/matrix; inhibitory neurons; macaque; midline thalamus; mice; rats; triads**

Significance Statement

The primate RE is a central node for memory and cognition through connections with the hippocampus and mPFC. As in rats or mice, the primate RE is a matrix-dominant thalamic nucleus, suggesting signal traffic to the upper cortical layers. Unlike rats or mice, the primate RE contains inhibitory neurons, synaptic specializations with the hippocampal pathway, and robust connections with the amygdala, suggesting unique adaptations. Convergence of hippocampal, mPFC, and amygdalar pathways in RE may help unravel a circuit basis for binding diverse signals for conscious flexible behaviors and the synthesis of memory with affective significance in primates, whereas disruption of distinct circuit nodes may occur in psychiatric disorders in humans.

Received Aug. 25, 2021; revised Nov. 22, 2021; accepted Dec. 2, 2021.

Author contributions: H.B. designed research; L.G.M., S.L.B., J.W., D.X., and J.G.B. performed research; M.K.P.J., L.G.M., S.L.B., D.X., J.G.B., and H.B. analyzed data; and M.K.P.J., L.G.M., and H.B. wrote the paper.

This work was supported by National Institutes of Health Grants R01MH057414 and R01MH117785. We thank Dr. Miguel Á. García Cabezas and Dr. Basilis Zikopoulos for assistance with photography and discussions and Jess Holz (MFA), Abigail Mark (BA), and Marcia Feinberg (MS) for expert help with electron microscopy and other technical assistance.

*M.K.P.J. and L.G.M. contributed equally to this work.

The authors declare no competing interests.

Correspondence should be addressed to Helen Barbas at barbas@bu.edu.

https://doi.org/10.1523/JNEUROSCI.1724-21.2021

Introduction

Situated directly above the third ventricle, the reuniens nucleus (RE) is the most ventral of the midline thalamic nuclei in rats, mice, and primates. Through strong bidirectional connections with the hippocampus and mPFC, studies in rats have revealed a pivotal role of RE in cognitive functions including spatial working memory, memory consolidation, and strategy shifting (Cholvin et al., 2013; Prasad et al., 2013; Saalmann, 2014; Ramanathan et al., 2018a; Hauer et al., 2019; Troyner and Bertoglio, 2021). Because the medial prefrontal cortex (mPFC) does not project directly to hippocampus, connections through RE provide a conduit for mPFC signals to enter the hippocampus (Cassel et al., 2013), a communication that is necessary for cognitive processes. The bulk of evidence on RE in rodents has been devoted to links with the hippocampus and mPFC (Dolleman-van der Weel et al., 2019).

Connections between RE and the hippocampus or the anterior cingulate cortex of mPFC have been described in monkeys as well (Amaral and Cowan, 1980; DeVito, 1980; Aggleton et al., 1986; Vogt et al., 1987; Barbas et al., 1991; Dermon and Barbas, 1994; Bachevalier et al., 1997; Chiba et al., 2001; Hsu and Price, 2007; Roberts et al., 2007). However, it is unclear to what extent the amygdala, which conveys signals pertaining to affective significance, is linked with RE in primates. This question arises because the primate amygdala is densely interconnected with the hippocampus and with mPFC (Ghashghaei et al., 2007; Wang and Barbas, 2018), consistent with the idea that cognitive and emotional processes are inextricably linked in primates (Barbas, 1995, 2000b; John et al., 2013).

In rodents, RE is characterized by its composition of projection neurons labeled with the calcium-binding proteins calbindin (CB) and calretinin (CR), but it lacks parvalbumin (PV) neurons (Arai et al., 1994; Bokor et al., 2002; Viena et al., 2021a). Thalamic CB and CR neurons give rise to the excitatory matrix thalamocortical system, which mostly innervates layers I–IIIa in wide axonal arbors and is thought to have a modulatory feedback-like role (Piantoni et al., 2016). The rat and mouse RE lacks the PV core thalamocortical system, which innervates the middle layers IIIb–V of cortex (Jones, 1998a,b; Vertes et al., 2015; Piantoni et al., 2016).

Extensive and elegant work in rats or mice has thus shed light on key anatomic and functional aspects of RE, placing it at the center of communication with structures associated with diverse aspects of memory and cognition. However, foundational questions about the composition and connections of the RE in primates remain unresolved. To what degree are chemoarchitectonic principles in the rat, including its composition and lack of inhibitory neurons, conserved in the macaque? Are the hippocampus, mPFC, A25, and the amygdala involved to the same extent in the macaque RE network?

Here, we studied the chemoarchitecture of the rhesus monkey RE, and its connections with the hippocampus, subgenual A25 of the mPFC, and the amygdala, including the largely unexplored synaptic interactions of these pathways. We found that several features of RE seen in rats and mice are conserved in the macaque. However, several chemoarchitectonic and connectional patterns emerged that reflect specializations in the rhesus monkey RE, including the presence of inhibitory neurons, some PV neurons, and strong connections with the amygdala. Moreover, hippocampal terminations entered into a privileged form of synaptic communication with excitatory projection neurons and local inhibitory neurons in macaque RE, as described for sensory relay nuclei (Famiglietti and Peters, 1972). This evidence suggests common patterns in thalamic processing across relay and high-order association nuclei associated with distinct pathways. These specializations may enable the synthesis of cognitive, mnemonic, and emotional processes that underlie behavioral flexibility in primates in processes that can be disrupted in several psychiatric diseases in humans (Dolleman-van der Weel and Witter, 2020).

Materials and Methods

Experimental design. Figure 1 provides an overview of our experimental design. First, to study the chemoarchitecture of RE, we used immunohistochemistry to label PV, CB, CR, and GABA in a series of sections through RE (Fig. 1*A*). We examined the distribution of immunolabeled neurons using exhaustive plotting. We then used immunohistochemistry for confocal and electron microscopy (EM) to study these chemoarchitectonic markers at high resolution.

Next, to study the connections between RE and A25, amygdala, or hippocampus (Fig. 1*B*), we injected bidirectional neural tracers into A25, amygdala, or hippocampus (Fig. 1*C*) and visualized them in RE using immunohistochemistry. This enabled us to map the distribution of anterogradely labeled axons and retrogradely labeled neurons in RE (Fig. 1*D*), representing incoming connections from the injection sites and the outgoing connections back to the injection sites, respectively. We then used stereologic sampling to quantify the density of tracer-labeled axonal terminations in the same series of sections. For each pathway, we performed an ultrastructural analysis from tissue immunohistochemically labeled for EM, offering a system-to-synapse approach to study these pathways at different scales (Fig. 1*E–H*).

Surgery, tracer injection, and perfusion. Table 1 lists the cases and analyses performed. Experiments were conducted on 12 rhesus monkeys (*Macaca mulatta*, 2–5.5 years old, $n = 8$ females) according to protocols approved by the Institutional Animal Care and Use Committee at Boston University School of Medicine, Harvard Medical School, New England Primate Research Center, in compliance with the National Institutes of Health *Guide for the Care and Use of Laboratory Animals*. Procedures were designed to minimize animal suffering. In each case, injections of multiple distinct tracers were placed to address questions in this and other unrelated studies, thus minimizing the number of animals needed for research.

For tracer injections, we conducted magnetic resonance imaging on each animal (after sedation by ketamine hydrochloride, 10–15 mg/kg, i.m.; anesthesia by propofol, loading dose 2.5–5 mg/kg, IV; continuous infusion rate 0.25–0.4 mg/kg/min) and placement in a stereotaxic apparatus (model #1430, David Kopf Instruments). MRI scans were registered to the stereotaxic space and used to calculate stereotaxic coordinates for injection of neural tracers.

About a week later, animals were sedated (as above) and then placed under general anesthesia (isoflurane, to a surgical level). We performed surgery under sterile conditions with continuous monitoring of respiratory rate, oxygen saturation, heart rate, and temperature. The head of each animal was placed in the stereotax to match its original MRI placement. A microdrive attachment was used to mount syringes for precise localization of planned injection coordinates. After exposing a small area of cortex above designated injection sites, Hamilton microsyringes (5 or 10 µl) were loaded with tracer (Invitrogen; Table 1), mounted, and guided toward the final injection site coordinates. We used molecular weight variants to aid in bidirectional tracing. The 3 kDA dextran amine variant is optimal for labeling of neuronal cell bodies and proximal dendrites, whereas the 10 kDA dextran amine variant is optimal for labeling axonal terminations. To avoid tracer leakage during insertion, we loaded syringes with a small bubble of air after aspiration of the tracer. Syringes were left at the site of injection for 5–10 min to allow for local diffusion of the tracer and prevent backward suction of the tracer during syringe retraction. Animals were monitored postoperatively and given antibiotics and analgesics as needed.

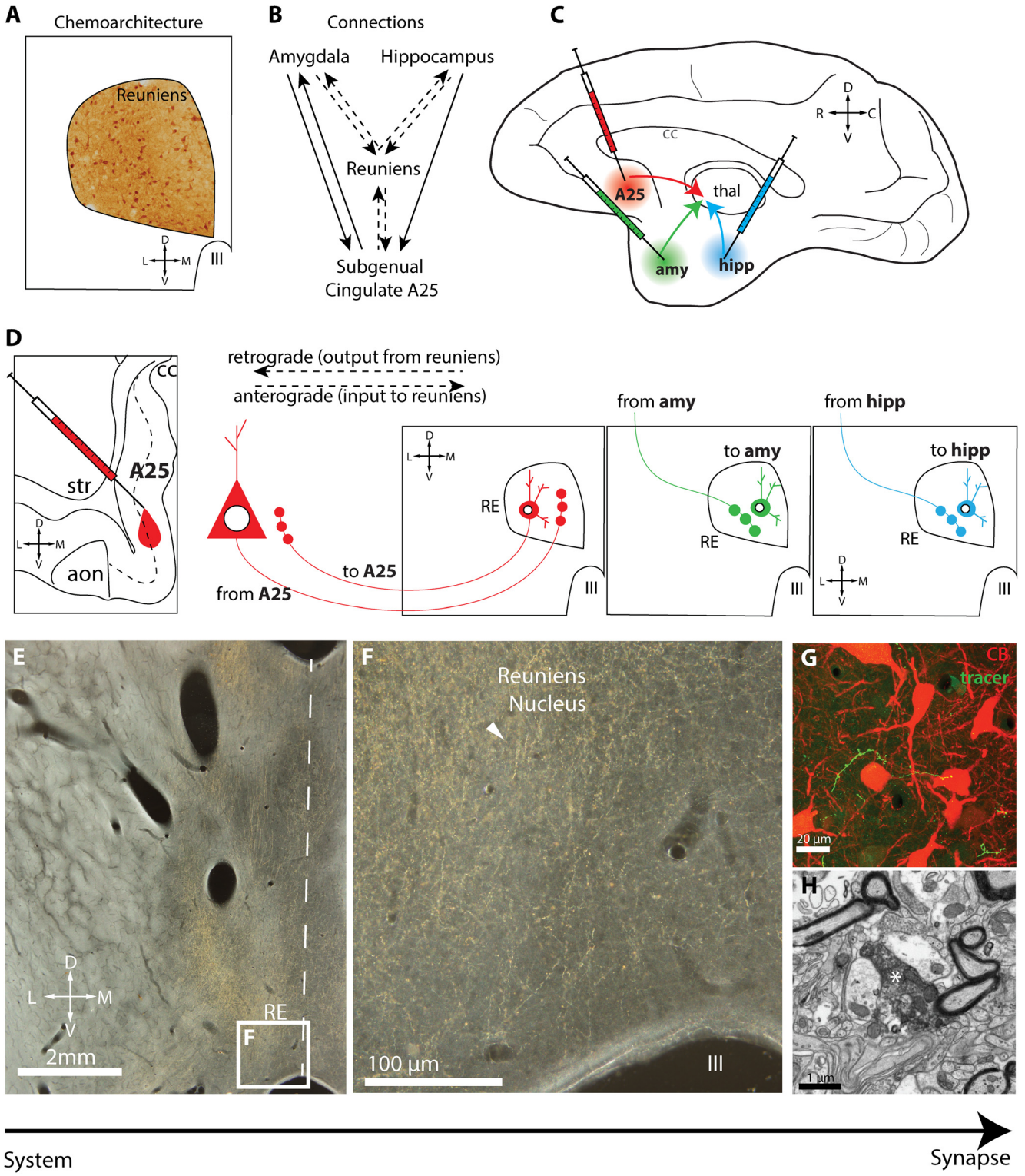

Figure 1. Experimental design. ***A***, Schematic depicts immunohistochemical labeling in the reuniens nucleus to characterize its chemoarchitecture for CB, CR, PV, and GABA. ***B***, Circuit organization schematic linking amygdala, hippocampus, and subgenual cingulate A25 with RE. Dashed lines indicate pathways under investigation in this study. ***C***, Schematic shows injection sites of neural tracers in A25, amygdala, and hippocampus. ***D***, Schematic depicts retrograde and anterograde transport from injection sites to RE. ***E***, Low-power photomicrograph taken using darkfield microscopy of tracer-labeled axonal terminations (yellow gold) in RE for pathway mapping and high-resolution ultrastructural investigation. Dashed line depicts midline. ***F***, Inset, From ***E***, tracer-labeled axonal terminations (yellow gold) in RE (white arrowhead). ***G***, Photomicrograph taken using confocal microscopy shows tracer-labeled axon terminations (green) comingling with matrix CB neurons (red) in RE. ***E–G***, Our strategy, which uses methods with increasing resolution to study the properties of these pathways, from system to synapse. ***H***, Photomicrograph taken using EM shows tracer-labeled axon termination (white asterisk) in RE. aon, Anterior olfactory nucleus; amy, amygdala; C, caudal; cc, corpus callosum; D, dorsal; hipp, hippocampus; III, third ventricle; L, lateral; M, medial; R, rostral; str, striatum; thal, thalamus; V, ventral.

Table 1. Case, injection site, tracer used, analysis performed

	Case	Hemisphere, sex, age	Injection site used	Tracer	Analysis
1	AJ	L + R, F	n/a	n/a	Photography of Nissl-stained sections
2	AZ	L + R, M	n/a	n/a	Photography and plotting of CB and PV neurons
3	BB	L, F, 2 y	Left-Amy (BM, BL, Ant) Right-Amy (BL, Ant, BM, Co)	BDA (3 kDA)	Bouton measurement (OM, L hemisphere)
4	BD	L + R, M, 2.5 y	Left-Amy (BL, Ce, La, BM) Right-Amy (Co, Me, BM, BL)	BDA	Bouton measurement (OM, L hemisphere), plotting of CB and PV neurons (R hemisphere)
5	BM	R, F, 3.5 y	Amy (BL)	FR (10 + 3 kDA)	Axon mapping, stereologic axon termination quantification, bouton measurement (OM), synaptic analysis (EM)
6	BQ	L, F, 3.5 y	Hipp (DG, CA1, ProS)	Alexa488 (10 kDA)	Axon mapping, stereologic axon termination quantification, bouton measurement (OM), synaptic analysis (EM), confocal photography
	BQ	L	A25 (anterior medial)	FR (10 + 3 kDA)	Bouton measurement (OM)
	BQ	R	Amy (BM and BL)	CBL, (10 + 3 kDA)	Synaptic analysis (EM)
7	BR	L, F, 3 y	A25 (posterior medial)	BDA (10 + 3 kDA)	Axon mapping, stereologic axon termination quantification, bouton measurement (OM), synaptic analysis (EM)
8	BS	L, F, 3.5 y	A25 (anterior medial)	LY (10 kDA)	Bouton measurement (OM), synaptic analysis (EM)
	BS	R	Hipp (CA1)	CBL (10 + 3 kDA)	Bouton measurement (OM)
9	BT	L, F, 4 y	Hipp (DG, CA1, CA3)	FE (10 + 3 kDA)	Axon mapping, stereologic axon termination quantification, bouton measurement (OM)
	BT	R	Amy (BL, BM)	BDA (10 + 3 kDA)	Axon mapping, stereologic axon termination quantification, bouton measurement (OM)
10	BU	L, M, 4 y	Hipp (DG, CA3, CA2, CA1)	CBL (10 + 3 kDA)	Synaptic analysis (EM)
	BU	R	A25 (anterior orbital)	FE (10 + 3 kDA)	Axon mapping, stereologic axon termination quantification, bouton measurement (OM)
11	BV	R, M, 4 y	n/a	n/a	Photography and plotting of CR neurons, photography and plotting of GABA neurons
12	BW	R, F, 5.5 y	Amy (BM, BL, Co)	FR (10 + 3 kDA)	Synaptic analysis (EM), plotting of CR neurons, photography and plotting of GABA neurons

Amy, Amygdala; BL, basolateral nucleus of the amygdala; BM, basomedial nucleus of the amygdala; CA, cornu ammonis; CBL, Cascade Blue; Ce, central nucleus of the amygdala; Co, cortical nucleus of the amygdala; DG, dentate gyrus; F, female; FE, Fluoroemerald; FR, Fluororuby; Hipp, hippocampus; kDA, kilodalton; L, left; La, lateral nucleus of the amygdala; LY, Lucifer yellow; Me, medial nucleus of the amygdala; n/a, not applicable; OM, optical microscopy; ProS, prosubiculum; R, right; y, year.

After a tracer propagation period of 18–20 d, animals were sedated, given a lethal dose of anesthetic (sodium pentobarbital, to effect), and transcardially perfused (4% paraformaldehyde, 0.2% glutaraldehyde in 0.1 M PBS, pH 7.4 used for cases BB, BD, BM, BQ, BR, BS, BT, BU, BV; 4% paraformaldehyde in 0.1 M cacodylate buffer, pH 7.4 used for case AJ; 4% paraformaldehyde in 0.1 M PBS, pH 7.4 used for cases AZ, BW). Brains were removed, photographed, cryoprotected in ascending sucrose solutions (10–25% sucrose, 0.05% sodium azide in 0.1 M PB, pH 7.4), frozen in −80°C isopentane, and sectioned on a freezing microtome (AO Scientific Instruments/Reichert Technologies) at 40 or 50 µm. We collected sections systematically into matched series and placed them in antifreeze (30% ethylene glycol, 30% glycerol, 0.05% sodium azide in 0.01 M PB, pH 7.4) for long-term storage.

Labeling procedures for brightfield, confocal, and electron microscopy. We processed free-floating sections with immunohistochemical techniques after first rinsing them of cryoprotectant using PB (0.1 M, pH 7.4). Procedures through the incubation of primary antibodies are as follows, whereas procedures after primary incubation differ and are described below. Antigen retrieval (not used for EM) was performed in sodium citrate solution (10 mM, pH 8.5; Sigma-Aldrich) using a 70–80°C water bath. Sections were rinsed and incubated in 0.05 M glycine (4°C, 1 h; Sigma-Aldrich) to bind free aldehydes. After rinsing, sections were incubated in 0.3% H_2O_2 in 0.1 M PB (30 min) to quench endogenous peroxidases (not used for fluorescence microscopy). In cases with a biotinylated dextran amine (BDA) injection not under study, we used Avidin/Biotin blocking solution (catalog #SP-2001, Vector Laboratories; RRID:AB_2336231) to block the biotin conjugate on the tracer (not necessary for fluorescence microscopy). Sections were then rinsed and blocked in preblocking solution, which contained 10% bovine serum albumin (BSA; Sigma-Aldrich), 10% normal serum of the secondary antibody host animal (donkey or goat; Sigma-Aldrich), 0.2% BSA-c (Aurion), 0.2% Triton X-100 (or brightfield and confocal microscopy; Sigma-Aldrich) or 0.025% reduced Triton-X100 (for EM; Roche Applied Science), and 0.1% cold-water fish gelatin (stabilization of ultrastructure for EM; Aurion). Sections were incubated with primary antibodies (Table 2), for 1–3 d, rinsed, then incubated in secondary antibodies (Table 2) for 3 h–1d. For control sections, we omitted the primary antibodies. Antibody incubations were enhanced by microwaving (2 min at 150 W, 4°C).

For brightfield microscopy, to visualize structures of interest after secondary antibody incubation, we rinsed sections and incubated them in avidin-biotin complex (ABC, 1:100 in 0.1 M PB; AB-HRP, catalog #PK-6100, Vector Laboratories; RRID: AB_2336827) and then processed with diaminobenzidine (DAB) for 1–3 min (catalog #SK-4100, Vector Laboratories; RRID: AB_2336382). Sections were mounted on gelatin-coated glass slides and dried. We counterstained some sections for Nissl (thionin stain) as previously described (García-Cabezas et al., 2016). Brightfield microscopy sections were coverslipped with Entellan (Sigma-Aldrich). We omitted primary antibodies for control experiments and found no evidence of immunolabeling.

For confocal microscopy (one case, BQ, hippocampus), after primary antibody incubation, we incubated sections in secondary antibodies for 3 h. The sections were then mounted, dried overnight, and coverslipped with ProLong Gold Antifade (catalog #36930, Invitrogen) and edges were hardened using fast-drying clear nail polish (Sally Hansen), which helps prevent the infiltration of air bubbles into the coverslipping medium.

For electron microscopy, in six cases, two for each pathway (A25, cases BR, BS; amygdala, cases BQ, BW; hippocampus, cases BQ, BU), we performed double- or triple-labeling EM immunohistochemical procedures to label the neural tracer and one or two other markers [PV, CB, CR, or glutamate decarboxylase-67 (GAD67)]. The tracer was always processed with DAB. For double labeling, the primary antibody for the second marker was paired with a gold-conjugated secondary antibody. For triple labeling, the third marker was visualized with tetramethylbenzidine (TMB). After primary antibody incubation (Table 2), we rinsed sections and incubated them in biotin-conjugated donkey anti-rabbit (for the tracer DAB, Table 2), and a donkey gold-conjugated secondary for the second marker. The sections were washed and underwent a rapid reduced concentration post fixation (3% glutaraldehyde, 1% paraformaldehyde in 0.1 M PB with 2 min microwave at 150 W, 4°C), followed by a glycine wash and rinse. We then silver enhanced the gold secondary antibodies using an enhancement conditioning solution (ECS, 1:10, 10 min; Enhancement Conditioning Solution 10_500.055, catalog #25830, Electron Microscopy Sciences), silver enhancement (90 min; R-GENT SE-EM kit, catalog #500.033, catalog #25520, Electron Microscopy Sciences), ECS again, and 0.1 M PB rinses. Then the tissue underwent ABC and DAB, as described above, to visualize the tracer.

Table 2. Antibodies used

Antibody	RRID	Use	Dilution
Mouse anti-PV, catalog #235, Swant	AB_10000343	Primary	1:2000
Goat anti-PV, catalog #214, Swant	AB_10000345	Primary	1:2000
Mouse anti-CB, catalog #300, Swant	AB_10000347	Primary	1:2000
Mouse anti-CR, catalog #6B3, Swant	AB_10000320	Primary	1:2000
Goat anti-CR, catalog #CG1, Swant	AB_10000342	Primary	1:2000
Rabbit anti-GABA, Immunostar, catalog #20095	AB_572233	Primary	1:1000
Rabbit anti-LY, catalog #A-5750, Molecular Probes	AB_2536190	Primary	1:800
Rabbit anti-Alexa488, catalog #A-11094, Molecular Probes	AB_221544	Primary	1:800
Rabbit anti-CBL, catalog #A-5760, Molecular Probes	AB_2536192	Primary	1:800
Rabbit anti-FR, catalog #A6397, Molecular Probes	AB_2536196	Primary	1:800
Rabbit anti-FE, catalog #A889, Molecular Probes	AB_221561	Primary	1:800
Mouse anti-GAD67, catalog #MAB5406, Millipore	AB_2278725	Primary	1:500
Biotinylated goat anti-mouse, catalog #BA-9200, Vector Laboratories	AB_2336171	Secondary	1:200
Peroxidase-AffiniPure donkey anti-goat, catalog #705–035-003, The Jackson Laboratory	AB_2340390	Secondary	1:200
Biotin-SP donkey anti-rabbit, catalog #711–065-152, The Jackson Laboratory	AB_2340593	Secondary	1:200
AlexaFluor 647 goat anti-mouse, catalog #A-21235, Thermo Fisher	AB_2535804	Secondary	1:100
AlexaFluor 488 goat anti-rabbit, catalog #A-11008, Thermo Fisher	AB_143165	Secondary	1:100
AlexaFluor 405 goat anti-rabbit, catalog #A-31556, Thermo Fisher	AB_221605	Secondary	1:100
Gold-conjugated donkey anti-mouse, catalog #800.322, Aurion		Secondary	1:50
Gold-conjugated donkey anti-goat, catalog #800.333, Aurion		Secondary	1:50

CBL, Cascade blue; FE, Fluoroemerald; FR, Fluororuby; LY, Lucifer yellow; RRID, Research Resource Identifier.

Sections were rinsed in 0.1 M PB, then underwent another 0.3% H_2O_2 to quench remaining peroxidases, and AB blocking to block remaining HRP-binding sites that could be bound during TMB. We then incubated the tissue with the third secondary antibody, which had a biotin conjugate, to visualize TMB. After incubation, sections underwent rinses, then TMB staining with stabilization using a DAB/cobalt chloride solution, as previously described (Medalla et al., 2007).

After completion of immunohistochemical procedures for EM, we performed microwave postfixation (6% glutaraldehyde, 2% paraformaldehyde in 0.1 M PB, 150 W, 15°C) until sample temperatures reached 30–35°C and then left the sections in the fixative to come to room temperature for 30 min, followed by 0.1 M PB rinses. We conducted EM processing using either a routine protocol for transmission EM (A25, case BS; amygdala, case BQ; hippocampus, cases BQ, BU) or a modified protocol optimized for high throughput block-face imaging (A25, case BR; amygdala, case BW). We have described routine and modified protocols for EM methods for ultrathin sectioning previously (Joyce et al., 2020; Wang et al., 2021).

Chemoarchitecture mapping and confocal microscopy. In four cases, we used immunohistochemical labeling for brightfield microscopy in a series of sections through RE to study PV, CB, CR, or GABA labeling (PV, CB, cases AZ, BD; CR, GABA, cases BV, BW; Table 1). Slides were placed on a microscope coupled with a semiautomated commercial system (Stereo Investigator; RRID:SCR_002526). We drew the boundaries of RE using Nissl staining according to the atlas of Olszewski (1952). To plot labeled neurons for each chemoarchitectonic marker, we used a meander-scan function at 200× to exhaustively plot all labeled neurons present in the RE for each section of the series.

In one case (hippocampus, case BQ), we processed RE for double immunofluorescence of the tracer and PV, CB, or CR. We imaged the tissue using a laser-scanning confocal microscope (Axio Observer Z1, LSM 880, Zeiss) at 630× (ZEN Digital Imaging for Light Microscopy, Zen 2.1 package; RRID:SCR_013672). Blue fluorophores were imaged with a Diode 405–30 laser, green fluorophores were imaged using a 488 nm argon ion laser, and far-red fluorophores were imaged with a 633 nm helium neon laser (all Zeiss). We acquired stacks of optical sections (0.31 µm step size). Stacks were deconvolved (Huygens Professional 17.10, Scientific Volume Imaging) to minimize the effect of the point spread function.

Pathway mapping and bouton diameter measurement using brightfield microscopy. In six cases, two from each pathway, we used immunohistochemical labeling for brightfield microscopy in a series of sections through RE to map tracer-labeled axon terminations coming from the injection sites and tracer-labeled neurons projecting to the injection sites (A25, cases BR, BU; amygdala, cases BM, BT; hippocampus, cases BT, BQ; Table 1). We viewed slides with a microscope coupled to a semiautomated commercial system (Stereo Investigator, RRID:SCR_002526). We drew the boundaries of RE using Nissl staining according to the atlas of Olszewski (1952).

To plot retrogradely labeled neurons for each injection site, we used a meander-scan function at 200× to exhaustively plot all tracer-labeled neurons present in RE for each section of each series. To map anterogradely labeled axonal terminations for each injection site, we used a meander-scan function at 1000× with oil immersion to exhaustively trace all tracer-labeled axons present in RE for each section of each series.

We then used unbiased stereological methods to quantify the density in RE of axonal terminations incoming from each injection site. We performed stereology using the optical fractionator method at 1000× with oil immersion via Stereo Investigator software, which uses systematic random sampling at regular intervals to extrapolate the number of markers and the volume for the region of interest (ROI; A25, cases BU, BR: disector 50 µm × 50 µm, grid size 250 µm × 250 µm, disector height 15 µm, guard zone of 2 µm; amygdala, cases BT, BM, and hippocampus, case BQ: disector 50 µm × 50 µm, grid size 250 µm x 250 µm, disector height 20 µm, guard zone 2 µm; hippocampus, case BT: disector size of 50 µm × 50 µm, grid size 150 µm × 150 µm, disector height 15 µm, guard zone 2 µm; Howard and Reed, 1998). These sampling rates yielded a coefficient of error <10%, as recommended (Gundersen, 1986). We computed the density of terminations by dividing the estimated number of terminations by the estimated volume of the nucleus for each case.

In 11 cases, 3–4 from each pathway, we used immunohistochemical labeling for brightfield microscopy in a series of sections through RE to visualize tracer-labeled axon terminations coming from the injection sites (A25, cases BQ, BR, BS, BU; amygdala, cases BB, BD, BM, BT; hippocampus, cases BQ, BS, BT; Table 1). We obtained brightfield microscopy *z* stacks with a step size of 0.5 µm. We imported stacks into the software program Synapse Web Reconstruct (RRID:SCR_002716; Fiala, 2005) or ImageJ (RRID:SCR_003070; Rasband, 1997) to measure the major diameter of all labeled terminations from the three pathways. We plotted the average distribution per pathway using a histogram and expressed the mean bouton diameter per pathway ± SEM.

EM: synaptic analysis of pathways and chemoarchitecture analysis. In six cases, two from each pathway, sections through RE were double or triple immunolabeled for EM and used for chemoarchitectonic analysis or pathway synaptic analysis (A25, cases BR, BS; amygdala, cases BQ, BW; hippocampus, cases BQ, BU; Table 1). We labeled neural tracers using DAB, which forms a dark precipitate that fills the cytoplasm of

neuronal elements containing tracer. We labeled PV, CB, CR, and GAD67 (a synthetic enzyme for GABA) using silver-enhanced gold, which forms small quanta that sometimes cluster, or TMB, which forms black stripes or crystalline-appearing clusters. Small cubes of tissue were placed on top of premade LX112 resin blocks in a drop of fresh resin. These blocks were then cured for ≥48 h at 60°C. For block-face imaging, cubes of tissue were affixed to aluminum pins using conductive epoxy glue (catalog #CW2400 Chemtronics). We used an ultramicrotome (Ultracut UCT, Leica Microsystems) to expose the surface of the tissue in the resin blocks or pins. After exposing the tissue, pins for block imaging were painted with conductive silver paint (catalog #16035, Ted Pella), which reduces charging artifacts in the scanning electron microscope. After the tissue was exposed on the resin blocks for the transmission electron microscope (TEM), we cut ~50 nm ultrathin sections and collected them sequentially on pioloform-coated copper slot grids to form series of 20–200 sections.

We imaged specimens using one of two microscopes. The first was an 80 kV TEM (100CX, JEOL) at 2000–33,000×. Boutons that had been labeled with DAB (a uniform black substrate in the cytoplasm) were located systematically and photographed for analysis using a digital camera (DigitalMicrograph, Gatan). EM stacks were aligned manually using the Reconstruct software.

For block-face imaging, we mounted pins into the 3View 2XP System (Gatan) coupled to a 1.5 kV scanning electron microscope (GeminiSEM 300, Zeiss). The surface of the pin was imaged using a backscatter detector, and then ROIs were selected based on the presence of labeled axons. ROIs were generally 20–25 µm × 20–25 µm fields imaged at 6.5 nm resolution. A built-in microtome then cut a 50 nm section from the surface of the pin, and the ROIs were imaged again. In this way, long series of 100–300 sections were imaged in sequence at each ROI. For series obtained using block-face imaging, we used an algorithm for alignment (GMS 3.0, Gatan). We imported EM stacks into Reconstruct.

Using Reconstruct, for stacks obtained from both TEM or the scanning electron microscope, we exhaustively measured all DAB-labeled boutons for major diameter to quantify bouton size. We also noted several qualitative factors in the synaptic interaction, (e.g., the presence or absence of mitochondria in a bouton).

Data analysis and statistics. We used SPSS for data analysis and statistics (IBM; RRID:SCR_002865). We used ANOVA to determine whether there were differences across pathways. If there were overall significant differences, we used *post hoc* Tukey tests for pair comparisons. We adjusted brightness, contrast, and saturation for photographs using ImageJ or Adobe Photoshop (RRID:SCR_014199) but did not retouch images. We prepared figures in Adobe Illustrator CC (RRID:SCR_010279).

Results

Figure 1 shows our experimental approach to study the architecture of RE and to investigate how pathways link A25, the amygdala, and hippocampus with RE. We used the Nissl stain to delineate the boundaries of RE in accord with the atlas of Olszewski (1952; Fig. 2). To study the chemoarchitecture, we stained a series of sections through RE for the calcium-binding proteins PV, CB, and CR or GABA (Fig. 1*A*).

We used neural tracers to study bidirectional pathways that link the RE with A25, amygdala, and hippocampus, as shown in Figure 1*B–D*. Using immunolabeling for the neural tracers in RE, we mapped the anterogradely labeled axon terminations (Fig. 1*E–G*) projecting from the injection sites to RE and the retrogradely labeled neuronal cell bodies that project from RE to these injection sites. We then used immunolabeling for EM to study ultrastructural specializations of synapses formed by axonal terminations in RE (Fig. 1*H*).

The RE contains mostly CB and CR excitatory neurons, some PV excitatory neurons, and GABAergic neurons

To create a comprehensive portrait of the chemoarchitecture of RE, we used immunohistochemistry to label the calcium-binding proteins PV, CB, and CR and determined their relative distributions in the nucleus in four cases ($n = 1$ female). PV, CB, and CR neurons label excitatory projection neurons in dorsal thalamus. PV excitatory neurons form the core of the thalamocortical projection system to the middle layers of cortex, whereas CB and CR neurons form the matrix of the thalamocortical projection system to layers I–IIIa and VI of cortex (Jones, 1998a; Zikopoulos and Barbas, 2007). Figure 3 shows photomicrographs of immunohistochemically labeled sections through the thalamus, and Figure 4 depicts plots of immunolabeled neurons positive for CB, PV, and CR. Numerous CB-positive neurons (Figs. 3*A–D*, 4*A*), seem to cluster in dorsal and lateral aspects of RE, much like in the rat (Lara-Vasquez et al., 2016; Cassel et al., 2021).

We found a sparse distribution of PV-positive neurons in both cases (Figs. 3*E–H*, 4*B*), and in one case there appeared to be small PV clusters more posteriorly (Fig. 4*B*, case BD, right). We also noted PV-positive neuronal processes, some of which were dendritic (Fig. 3*H*,*Q*,*T*). Some other PV neuronal processes may be axons belonging to the entirely inhibitory thalamic reticular nucleus (TRN), which contains inhibitory PV neurons that innervate the nuclei of the dorsal thalamus.

Although studies in the primate thalamus have focused mainly on PV and CB relay neurons, we previously found a small pathway of CR thalamocortical projections from the magnocellular sector of the mediodorsal nucleus (MDmc) to the posterior orbitofrontal cortex (Timbie and Barbas, 2015). Here, we found evidence of many CR-positive neurons in RE using brightfield (Figs. 3*I–L*, 4*C*), confocal (Fig. 3*S*), and electron microscopy (Fig. 3*V*). Unlike the CB neurons, which were clustered, CR neurons seem to have a consistent distribution throughout the nucleus (Fig. 4*C*).

Using double labeling of the tracers and PV, CB, or CR for fluorescence microscopy, we found evidence that retrogradely labeled neurons that project to the injection sites were positive for CB or CR (e.g., for hippocampus, Fig. 3*R*,*S*, white arrowheads). This analysis was not exhaustive and does not rule out the possibility that PV-positive neurons project to these regions as well or that some neurons may be immunopositive for both CB and CR. Together, our data suggest that the primate RE nucleus is a matrix-dominant thalamocortical projection system with a small core component.

We also examined the inhibitory chemoarchitecture in RE (Fig. 3*M–P*). We found a moderate but consistent distribution of GABA-ergic cell bodies in the nucleus (Fig. 4*D*). In one case (Fig. 4*D*, BV, left), GABA-ergic neurons tended to be less dense ventrally. We also saw dendrites in RE that were labeled for GAD-67, a synthetic enzyme for GABA (Fig. 3*W*); they contained pleomorphic vesicles, which is typical of inhibitory dendrites in dorsal thalamus.

Pathway tracing: Injection sites

We then studied bidirectional pathways that link RE with the hippocampus, A25, and amygdala. Figure 5 depicts the injection sites. In four cases ($n = 3$ female), we injected the hippocampus with a bidirectional neural tracer (Fig. 5*A*). Table 1 lists the hemisphere, age, sex, tracer, and hippocampal subfields for each injection. All injections included at least part of hippocampal CA1, as previously described for a different study (Wang et al., 2021).

Figure 5*B* depicts injection sites in A25 in four cases ($n = 3$ female; Table 1). Three of the injections were made into medial A25, ranging from anterior to the posterior aspects (cases BS, BQ, BR). One injection was in anterior orbital A25 (case BU).

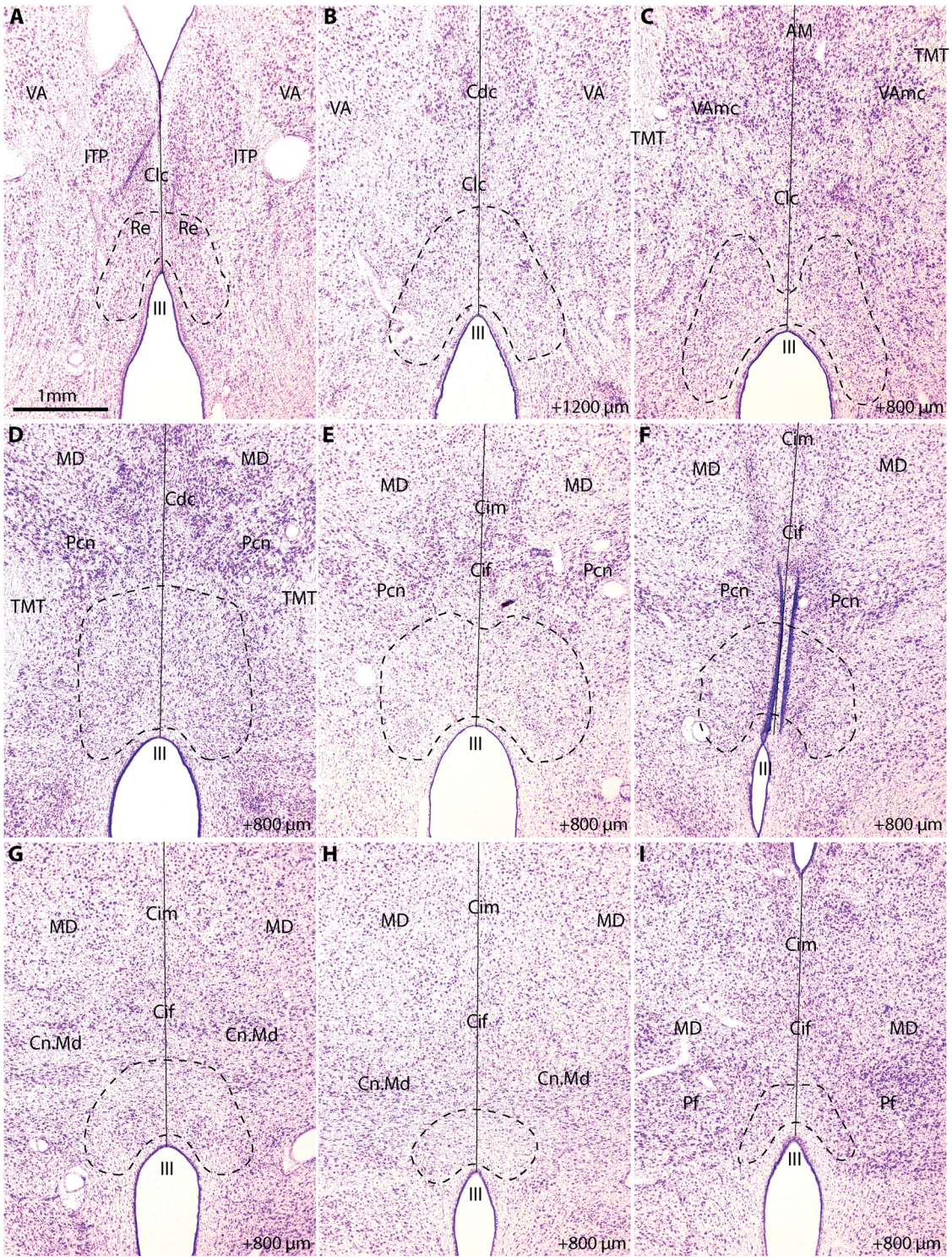

Figure 2. Cytoarchitecture of the reuniens nucleus. ***A***, Low-power photomicrograph of a coronal section through the rostral thalamus stained for Nissl. ***B***, Photomicrograph of a coronal section stained for Nissl, 1200 µm posterior to ***A***. ***C–I***, Photomicrographs of coronal sections 800 µm posterior to previous image. Dashed line indicates boundaries of RE according to Olszewski (1952). Solid line indicates the midline. AM, Anterior medialis nucleus; Cdc, nucleus centralis densocellularis; Cif, nucleus centralis inferior; Cim, nucleus centralis intermedialis; Clc, nucleus centralis latocellularis; Cn.Md, nucleus centrum medianum; III, third ventricle; ITP, inferior thalamic peduncle; MD, medialis dorsalis nucleus; Pcn, nucleus paracentralis; Pf, nucleus parafascicularis; TMT, mamillo-thalamic tract; VA, nucleus ventralis anterior; VAmc, nucleus ventralis anterior pars magnocellularis.

These cases have been used in a previous unrelated study (Joyce and Barbas, 2018), and one is reported here for the first time (Fig. 5*C*).

Figure 5*D* depicts injection sites in the amygdala in six cases (n = 5 females; Table 1). Most injection sites were in the medial aspect of the amygdala, targeting the basomedial (also known as accessory basal) and basolateral nuclei. Most have been used in previous unrelated studies (Ghashghaei et al., 2007; Hoistad and Barbas, 2008; Zikopoulos and Barbas, 2012; Timbie and Barbas, 2014; Wang and Barbas, 2018), whereas two are reported for the first time here (Fig. 5*E*,*F*).

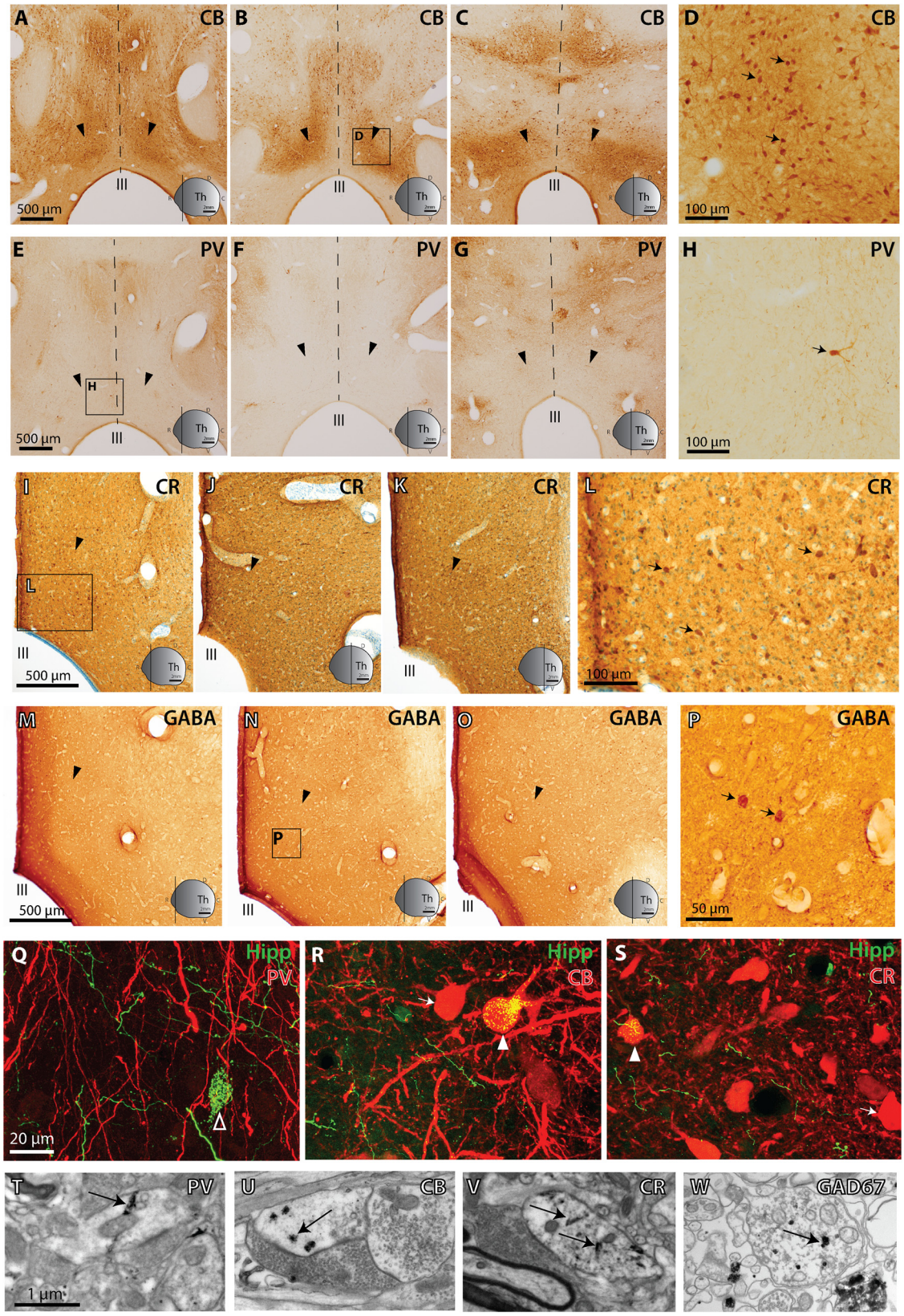

Figure 3. Chemoarchitecture of the reuniens nucleus. ***A–C***, Brightfield photomicrographs of coronal sections immunolabeled for CB through the ventral midline thalamic nuclei. Dashed line denotes midline, and black arrowheads point to the RE. Right, bottom, Plane of section through thalamus (Th). ***D***, Inset, From ***B***, black arrows indicate darkly labeled CB neurons. ***E–G***, Brightfield photomicrographs of coronal sections immunolabeled for PV through the ventral midline thalamic nuclei. ***H***, Inset, From ***E***, black arrow indicates darkly labeled PV cell. The surrounding area contains PV+ labeled processes, some of which are likely axons from the TRN. ***I–K***, Brightfield photomicrographs of coronal sections immunolabeled for CR (brown) and counterstained for Nissl (blue) through the ventral midline thalamic nuclei. ***L***, Inset, From ***I***, black arrows indicate darkly labeled CR neurons. ***M–O***, Brightfield photomicrographs of coronal sections immunolabeled for GABA through the ventral midline thalamic nuclei. ***P***, Inset, From ***N***, black arrows indicate darkly labeled GABA cells. ***Q***, Collapsed confocal microscopy *z* stack (maximum projection) shows tracer-labeled axon terminations (green; here, BQ-Alexa488 injected in hippocampus, as in ***R***, ***S***. comingling with PV-positive neuronal processes (red) in RE. Empty white

Patterns of connections between hippocampus, amygdala, and A25 with RE

To study the features of pathways from A25, amygdala, and hippocampus to RE, we immunolabeled neural tracers for brightfield microscopy in series of sections through RE and systematically mapped them. Figure 6 depicts the pattern of axon terminations from A25, amygdala, and hippocampus through RE. Figure 7 shows the pattern of retrogradely labeled neurons through RE that project to the same injection sites. The posterior medial A25 injection (Fig. 6*A–D*) showed dense terminations in rostral RE and was sparser in caudal RE. Neurons projecting from RE to posterior medial A25 were also concentrated in the rostral RE (Fig. 7*C*), consistent with the distribution of axonal terminations from this injection site.

The anterior orbital A25 injection (Fig. 6*A*,*E–G*) showed sparse terminations throughout rostral RE with more dense terminations in caudal aspects. This is in contrast with the distribution of tracer-labeled neurons that project back to this injection site from RE, which were denser in the rostral parts of the nucleus (Fig. 7*E*).

Pathways from two injection sites in amygdala terminated with relatively consistent density throughout the rostral to caudal extent of RE (Fig. 6*H–N*). Consistent with the distribution of axonal terminations from the amygdala, neurons projecting back to the amygdala from RE were distributed relatively consistently through the rostral to caudal parts of RE (Fig. 7*F–J*).

Terminations from the hippocampus were denser in rostral parts of RE (Fig. 6*O–V*), especially when the subicular complex was included in the injection site (Fig. 6*S–V*, case BQ). Neurons projecting back to the respective hippocampal sites were denser in rostral and sparser toward the caudal parts of RE (Fig. 7*K–P*).

Hippocampal, amygdala, and A25 axonal terminations are comparable in size in RE

Bouton size is correlated with synaptic efficacy (Stevens, 2004; Rollenhagen and Lubke, 2006). To investigate whether A25, hippocampus, or amygdala terminations differed in size, we used immunolabeling to convert the neural tracers for brightfield microscopy, as described above (Fig. 8*A–C*). We obtained *z* stacks through the depth of tissue at 1000× and measured the major diameters of axonal terminations (Fig. 8*D*). This analysis showed that the mean diameter of axonal terminations from A25, amygdala, and hippocampus was not significantly different (Fig. 8*G*; $F_{(2,8)} = 0.004$, $p = 0.996$, ANOVA).

Specializations of synapses from hippocampal, amygdala, and A25 in RE

To study how axon terminations from A25, amygdala, and hippocampus form synapses in RE, we immunolabeled the neural tracers for EM and collected serial ultrathin sections through RE. We found that in one case, amygdalar axons were distinguished by forming synapses from successive boutons on one axon with the same postsynaptic structure (Fig. 9; case BQ, 4 occurrences in $n = 60$ boutons).

We found a different set of ultrastructural specializations in both cases used for the hippocampal pathway to RE in which axon terminations formed multisynaptic complexes with excitatory and inhibitory dendrites in RE (Figs. 10, 11). In one case (Fig. 10, BU), a hippocampal termination (blue) formed synapses with four distinct postsynaptic structures, including a synapse with an excitatory CB-positive thalamic relay dendritic shaft (green), a thorn from the same dendrite, an inhibitory dendrite that contained pleomorphic vesicles (pink-orange), and two other postsynaptic structures, likely inhibitory dendrites (purple, yellow). In another case (Fig. 11, BQ), shown here as a 3D reconstruction from serial EM, a hippocampal termination (blue) formed synapses with five distinct postsynaptic structures, including the shaft and thorns of CR-positive thalamic relay dendrite (light green) and four inhibitory dendrites (orange or pink).

Figure 12 depicts the quantitative ultrastructural results. Bouton diameters were comparable across pathways (Fig. 12*A*,*B*; $F_{(2,3)} = 2.367$, $p = 0.242$, ANOVA), although they were bigger than those measured using optical microscopy. The difference may be because of the level of resolution of the two methods. For example, at the optical microscopy level we look for axon varicosities that are suggestive of axonal terminations, whereas when using EM we can confirm the classification of an axonal termination by using the presence of a synapse. A second reason for the difference may be the smaller sample sizes that are an unavoidable limitation for analysis at the level of EM.

The tendency to form synapses on thorns, the cytoplasmic extensions on excitatory thalamic relay dendrites, was somewhat higher for the amygdalar pathway, but the differences were not significant across the three pathways (Fig. 12*C*; $F_{(2,3)} = 0.962$, $p = 0.476$, ANOVA). Axon terminations from the amygdalar pathway were significantly more likely to contain mitochondria (Fig. 12*D*; $F_{(2,3)} = 66.106$, $p = 0.003$, ANOVA; *post hoc* Tukey's test, amygdala and hippocampus, $p = 0.003$; amygdala and A25, $p = 0.008$). Axon terminations from the hippocampus tended to be more likely to form perforated synapses or be multisynaptic, although these differences were not significant across pathways (Fig. 12*E*,*F*; multisynaptic, $F_{(2,3)} = 2.313$, $p = 0.247$, ANOVA; perforated synapses, $F_{(2,3)} = 2.122$, $p = 0.267$, ANOVA).

Discussion

Several RE features seen in rats and mice are conserved in the rhesus macaque, including connections with hippocampus and mPFC. As in rats (Varela et al., 2014), hippocampal connections in RE are denser rostrally. Further, the primate RE is mostly populated with CB and CR projection neurons as in rats (Dolleman-van der Weel et al., 2019).

Our findings also reveal macaque specializations in RE neurochemical composition, connections, and synaptic interactions.

←

arrowhead indicates a retrogradely labeled neuron. Scale bar applies to ***R***, ***S***. ***R***, Collapsed *z* stack shows tracer-labeled axon terminations from hippocampus (green) comingling with CB-positive neurons and processes (red) in RE. White arrowhead indicates a CB-positive retrogradely labeled neuron (small green-yellow granules indicate neural tracer colabeling). White arrow indicates darkly labeled CB neuron. ***S***, Collapsed *z* stack shows tracer-labeled axon terminations from hippocampus (green) comingling with CR-positive neurons and processes (red) in the RE. White arrowhead indicates a CR-positive retrogradely labeled neuron. White arrow indicates darkly labeled CR neuron. ***T***, Electron photomicrograph of a PV-positive dendrite in RE immunolabeled with TMB (black stripe, black arrow). An unlabeled axon terminal forms an asymmetric (excitatory) synapse along the lower right aspect of the dendrite. Scale bar applies to ***U-W***. ***U***, Electron photomicrograph of a CB-positive dendrite in RE immunolabeled with gold (round black clusters, black arrow). An unlabeled axon terminal forms a perforated asymmetric (excitatory) synapse along the lower aspect of the dendrite. ***V***, Electron photomicrograph of a CR-positive dendrite in RE immunolabeled with TMB (black smears, black arrows). An unlabeled axon terminal forms an asymmetric (excitatory) synapse along the lower left aspect of the dendrite ***W***, Electron photomicrograph of a GAD67-positive dendrite in RE immunolabeled with gold (round black clusters, black arrow). C, Caudal; D, dorsal; Hipp, hippocampus; III, third ventricle; R, rostral; Th, thalamus; V, ventral.

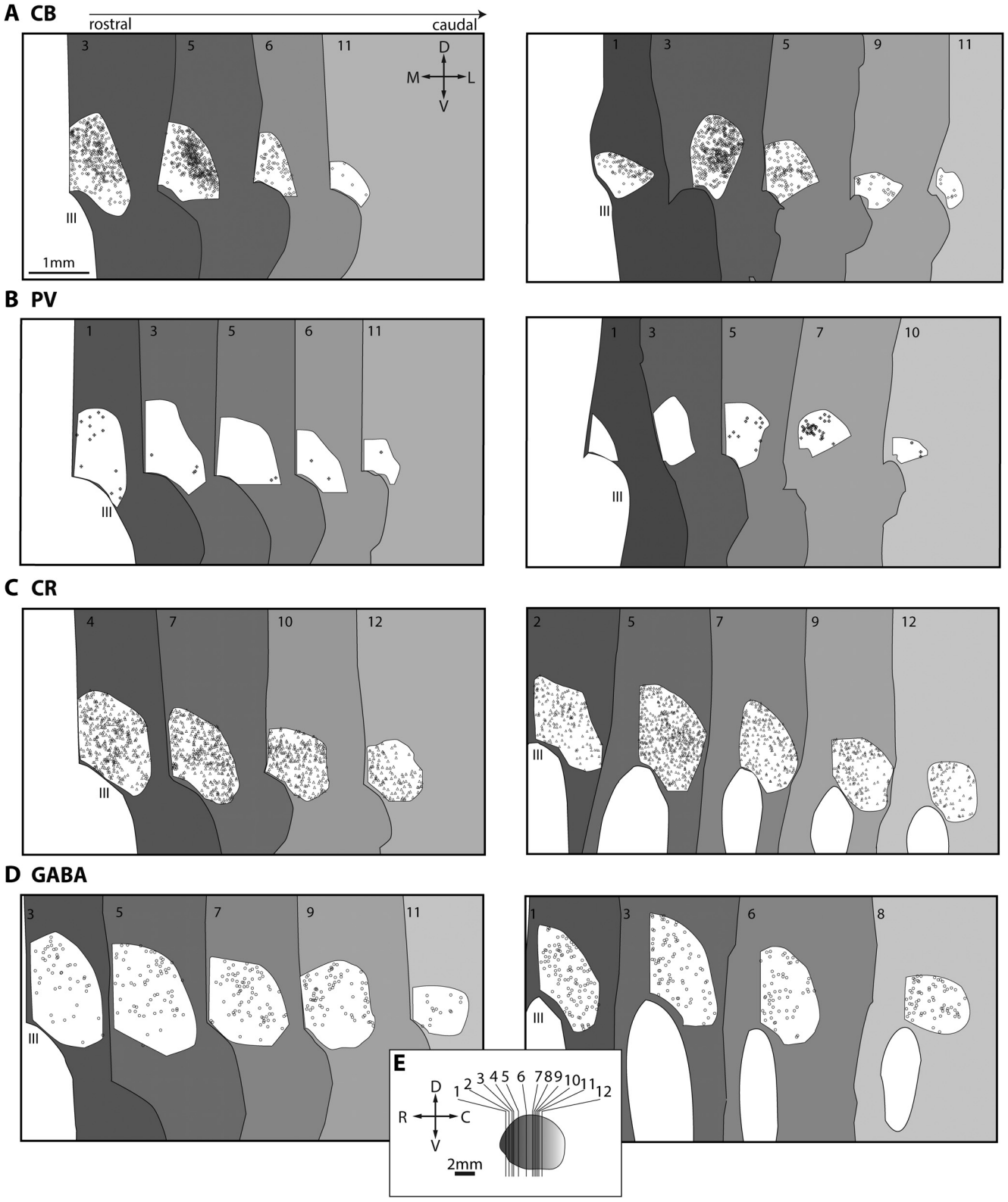

Figure 4. Maps of the PV, CB, CR, and GABA neurons in reuniens nucleus. Coronal sections through RE are depicted from rostral (dark gray) to caudal (light gray). ***A***, CB neurons in RE in two cases (left, AZ; right, BD). Compass and scale apply in ***A–D***. ***B***, PV neurons RE in two cases (left, AZ; right, BD). ***C***, CR neurons in RE in two cases (left, BV; right, BW). ***D***, GABA neurons in RE in two cases (left, BV; right, BW). ***E***, Planes of cut for plots in ***A–D***. C, Caudal; D, dorsal; III, third ventricle; L, lateral; M, medial; R, rostral; V, ventral.

First, we found that the amygdala projects robustly throughout the rostro-caudal extent of RE, unlike the sparse projections in rodents (Herkenham, 1978; McKenna and Vertes, 2004; Vertes et al., 2006). Second, we found a consistent scatter of PV neurons in RE, which are not found in rats or mice (Cassel et al., 2021). Third, we found GABAergic neurons in RE, not seen in rodents (Ferraris et al., 2021). Fourth, these inhibitory neurons in RE entered into multisynaptic complexes

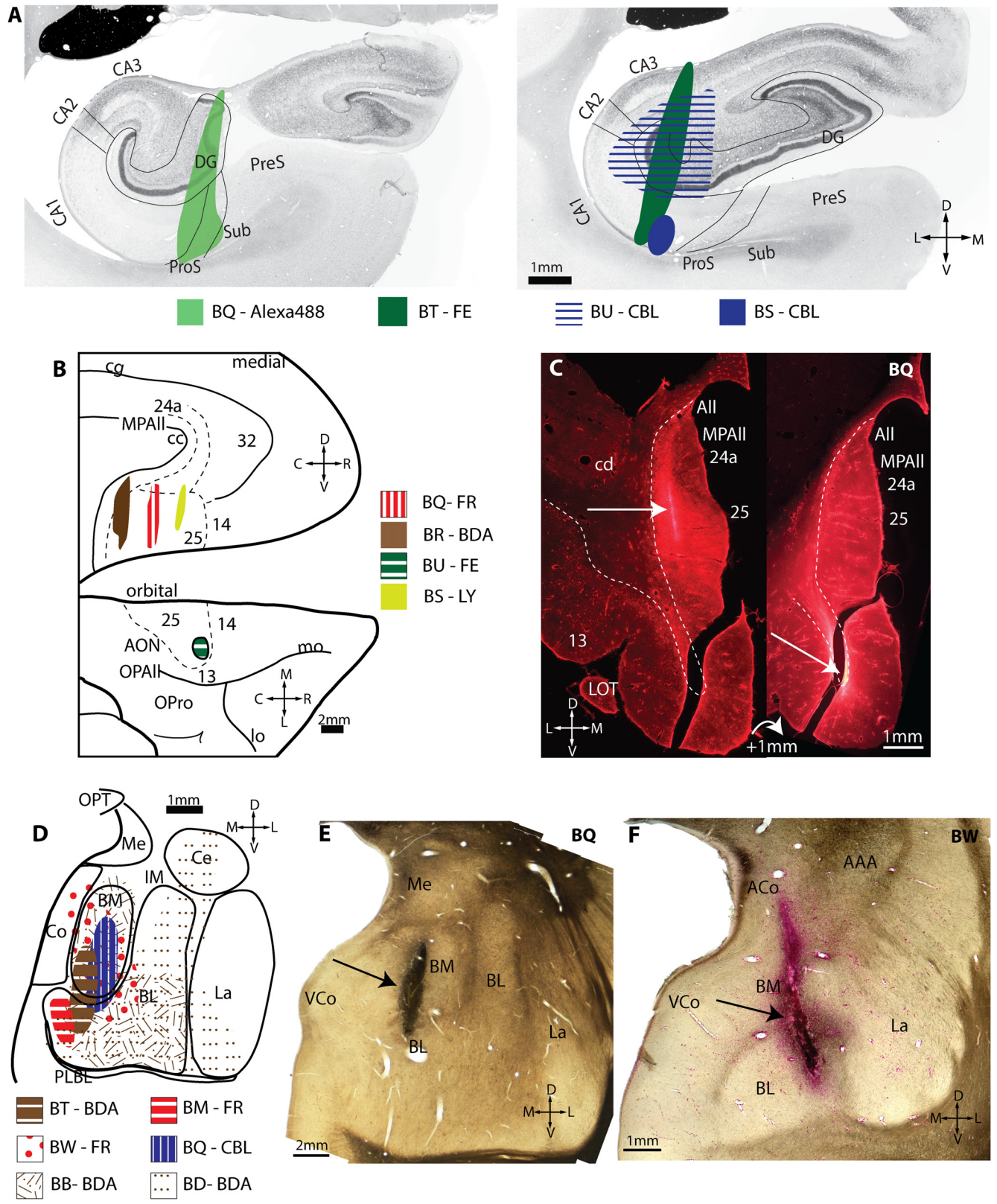

Figure 5. Injection sites in hippocampus, A25, and amygdala. ***A***, Injection sites in two planes through the hippocampus. ***B***, Injection sites in normalized A25 space. Top, Medial surface of the rhesus monkey brain. Bottom, Orbital surface. ***C***, Fluorescent photomicrographs of two coronal sections through A25 depict the extent of the injection site in medial A25. Dashed line delineates the boundary with the white matter. White arrow indicates injection site. ***D***, Injection sites in normalized amygdala space. ***E–F***, Brightfield photographs of wet-mounted coronal sections through the amygdala depict injection sites (black arrows). AAA, Anterior amygdaloid area; ACo, anterior cortical nucleus of amygdala; All, Allocortex; AON, anterior olfactory nucleus; BL, basolateral nucleus of the amygdala; BM, basomedial nucleus of the amygdala; C, caudal; CA, cornu ammonis; CBL, Cascade Blue; cc, corpus callosum; cd, caudate; Ce, central nucleus of the amygdala; cg, cingulate sulcus; Co, cortical nucleus of the amygdala; D, dorsal; DG, dentate gyrus; FE, Fluoroemerald; FR, Fluororuby; IM, intercalated masses of the amygdala; L, lateral; La, lateral nucleus of the amygdala; lo, lateral orbital sulcus; LOT, lateral olfactory tract; LY, Lucifer yellow; M, medial; Me, medial nucleus of the amygdala; mo, medial orbital sulcus; MPAll, medial

specifically with hippocampal terminals and local projection neurons as elaborated below.

Common and specialized connections of RE in primates and rodents

There is evidence that the rodent hippocampus provides signals about the contextual significance of memories to mPFC for cognitive operations (Mathiasen et al., 2020). In the absence of a direct pathway from mPFC to hippocampus, prefrontal signals must be conveyed to hippocampus through a third area, such as the entorhinal cortex or RE, both of which have bidirectional connections with the hippocampus and mPFC (Barbas, 2000a; Varela et al., 2014). This tripartite system involving RE has been associated with memory, ranging from acquisition to extinction (Troyner and Bertoglio, 2021), and for sequential events (Jayachandran et al., 2019). In addition, RE mediates hippocampus–mPFC synchronization during slow-wave sleep, promoting information transfer and memory consolidation (Roy et al., 2017; Hauer et al., 2019).

Connections from hippocampus likely transmit contextual information to RE needed to flexibly gauge behavioral responses in a changing environment, such as learning to avoid stimuli that signal danger and extinguish fear responses when the stimuli no longer signify danger (Ramanathan et al., 2018a). The centrality of RE for contextual significance of memories is exemplified by the consequences after its destruction, leading to degraded mnemonic specificity and overgeneralization (Xu and Sudhof, 2013; Ramanathan et al., 2018b; Ramanathan and Maren, 2019; Linley et al., 2021; Silva et al., 2021; Troyner and Bertoglio, 2021).

Yet, behavioral paradigms that elicit fear also implicate structures associated with emotion, like the amygdala and mPFC. However, connections between RE and amygdala in rats and mice are sparse or moderate (Herkenham, 1978; McKenna and Vertes, 2004; Hoover and Vertes, 2007; Scheel et al., 2020) and more compartmentalized to medial and cortical nuclei, which have endocrine and reproductive functions (De Olmos, 1990). In contrast, connections between RE and amygdala in rhesus monkeys were robust, with amygdala terminations distributed more extensively within RE than the hippocampal or A25 pathways. Ubiquitous amygdalar projections to RE from basolateral and basomedial nuclei, which are also strongly connected with mPFC and orbitofrontal cortex (Ghashghaei et al., 2007), may have multiple roles. During relatively safe situations, the amygdala may provide ongoing information to RE about affective significance (John et al., 2016). Along with internal state information from A25 and contextual information from hippocampus, both of which are also innervated by the amygdala, the convergent circuitry may allow integration for flexible adjustment of strategy as behavioral contingencies change (Dolleman-van der Weel et al., 2019).

Beyond their expansive terminations in RE, amygdalar boutons were more likely to contain mitochondria than the other pathways, suggesting high activity (Devine and Kittler, 2018). In addition, amygdalar terminals from the same axon formed synapses on the same postsynaptic sites in RE, suggesting high efficiency for activating postsynaptic sites, presumably needed when survival is at stake (John et al., 2016). An outsized input weight may ensure that important signals are faithfully received. This pattern is reminiscent of the robust amygdalar pathway to hippocampal CA3 (Wang and Barbas, 2018), which influences the internal processing of hippocampus. The primate amygdala also innervates hippocampal CA1, which is also the target of a pathway from RE along with the subiculum (Wouterlood et al., 1990; Vertes et al., 2006). CA1 receives projections from CA3 and projects out of the hippocampus. These findings demonstrate that the amygdala can influence the internal circuitry as well as the output of the hippocampus.

In the hippocampal–RE system, the primary cortical target in mPFC may be A25, which receives the bulk of hippocampal projections (Wang et al., 2021) and also has strong bidirectional connections with the amygdala (Ghashghaei et al., 2007). A25 may impart mood- or goal-related information to RE using convergent contextual signals from the hippocampus and signals pertaining to affective relevance from the amygdala, contributing to greater cognitive flexibility and emotional range seen in primates.

Inhibitory neurons in RE and the dual thalamocortical system

Inhibitory GABAergic neurons in the macaque RE reflect another specialization not found in rats or mice (Ferraris et al., 2021) but seen also in some other species, for example, cats (Jones, 2009). Significantly, some hippocampal terminations formed synaptic complexes with excitatory and inhibitory dendrites in RE, akin to triads formed by retinal afferents with local excitatory and inhibitory dendrites in the lateral geniculate nucleus (LGN), as in other sensory thalamic nuclei (Famiglietti and Peters, 1972; Jones, 1985). We found this specialized synaptic interaction between some hippocampal boutons and inhibitory neurons in RE but not for the amygdala or A25 pathways. Recently, we found that large amygdalar terminals uniquely form complex synaptic triads in thalamic MDmc nucleus but not in midline thalamic nuclei that also receive strong amygdalar pathways (Timbie et al., 2020). Specific structures thus seem matched with specific thalamic nuclei for privileged triadic communication, aligning the hippocampus with RE and the amygdala with MDmc (Timbie et al., 2020). This evidence suggests that synaptic triads may be a common feature across the macaque thalamus, a principle we can now extend to high-order thalamic nuclei, which were thought to be distinct (Sherman, 2012).

In triads, thalamic projection neurons receive monosynaptic excitation from an afferent pathway and disynaptic inhibition through the dendrites of local interneurons. The triadic architecture enriches the firing dynamics of projection neurons, including bursting activity, a thalamic mode that increases the gain (Kim and McCormick, 1998; Sherman, 2004) and facilitates transmission to cortex (Alitto et al., 2019). In both the amygdalar pathway to MDmc and the hippocampal to RE, multisynaptic complexes were more elaborate than the triads seen by retinal pathways in LGN, suggesting even more intricate neuronal dynamics that require future study.

Much like rats and mice, the primate RE is a predominantly matrix nucleus. In primates, matrix CB thalamocortical projections terminate in the superficial layers with a large horizontal reach. In contrast, core PV thalamocortical projections terminate focally in the middle cortical layers (Jones, 1998b, 2001; Zikopoulos and Barbas, 2007). The scattered PV neurons in the primate RE may represent a small core thalamocortical system. Both PV and CB thalamic neurons receive substantial cortical

←

periallocortex; OPAll, orbital periallocortex; OPro, orbital proisocortex; OPT, optic tract; P, posterior; PLBL, paralaminar basolateral nucleus of the amygdala; ProS, prosubiculum; PreS, presubiculum; R, rostral; Sub, subiculum; uCA, uncal cornu ammonis; V, ventral; VCo, ventral cortical nucleus of the amygdala.

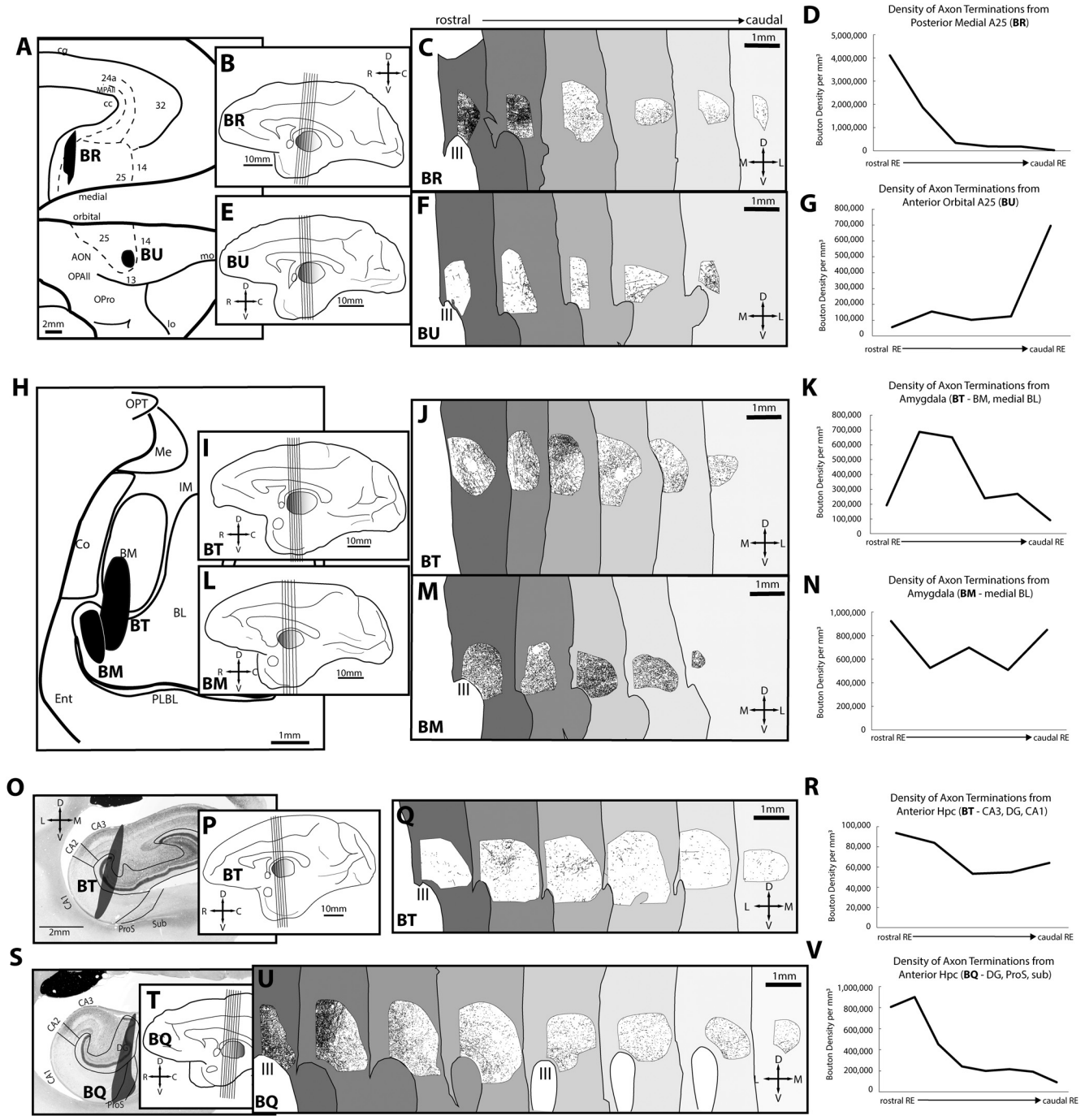

Figure 6. Axonal terminations in reuniens from A25, amygdala, and hippocampus. ***A***, Normalized A25 space depicts location of injection sites (black) used to map axonal terminations. Case BR features a posterior medial injection site; case BU features an anterior orbital injection site. Dashed lines depict areal boundaries. ***B***, Medial surface (case BR). Lines depict planes of cut for sections seen in ***C***. ***C***, Individual axons traced in RE depict the termination pattern (case BR) from rostral levels (left, dark gray) to caudal levels (light gray). ***D***, Stereologic density of axonal terminations from rostral (left) to caudal (right) RE sections (case BR). ***E–G***, Organization as above, but for case BU in A25. ***H***, Normalized amygdala space depicts location of injection sites (black) used to map axonal terminations. One case (BT) featured an injection in the basomedial (also known as accessory basal) and ventral medial sector of the basolateral nucleus. The other case (BM) featured an injection in the ventral medial sector of the basolateral nucleus. ***I–K***, Organization as above, but for case BT in amygdala. ***L–N***, As above, but for case BM in amygdala. ***O***, Injection site (black) in the hippocampus (case BT) used to map axonal terminations after tracer injection in CA3, DG, and CA1. ***P–R***, As above, but for case BT in hippocampus. ***S***, Injection site (black) in the hippocampus (case BQ) used to map axonal terminations after tracer injection in CA1, DG, prosubiculum, and subiculum. ***T–V***, As above, but for case BQ in hippocampus. AON, Anterior olfactory nucleus; BL, basolateral nucleus of amygdala; BM, basomedial nucleus of the amygdala; C, caudal; CA, cornu ammonis; Ce, central nucleus of the amygdala; cg, cingulate sulcus; Co, cortical nucleus of the amygdala; D, dorsal; DG, dentate gyrus; Ent, entorhinal cortex; III, third ventricle; IM, intercalated masses of the amygdala; L, lateral; La, lateral nucleus of the amygdala; lo, lateral orbital sulcus; M, medial; Me, medial nucleus of amygdala; mo, medial orbital sulcus; MPAll, medial periallocortex; OPAll, orbital periallocortex (agranular); OPro, orbital proisocortex (dysgranular); OPT, optic tract; PLBL, paralaminar basolateral nucleus of the amygdala; ProS, prosubiculum; R, rostral; Sub, subiculum; V, ventral.

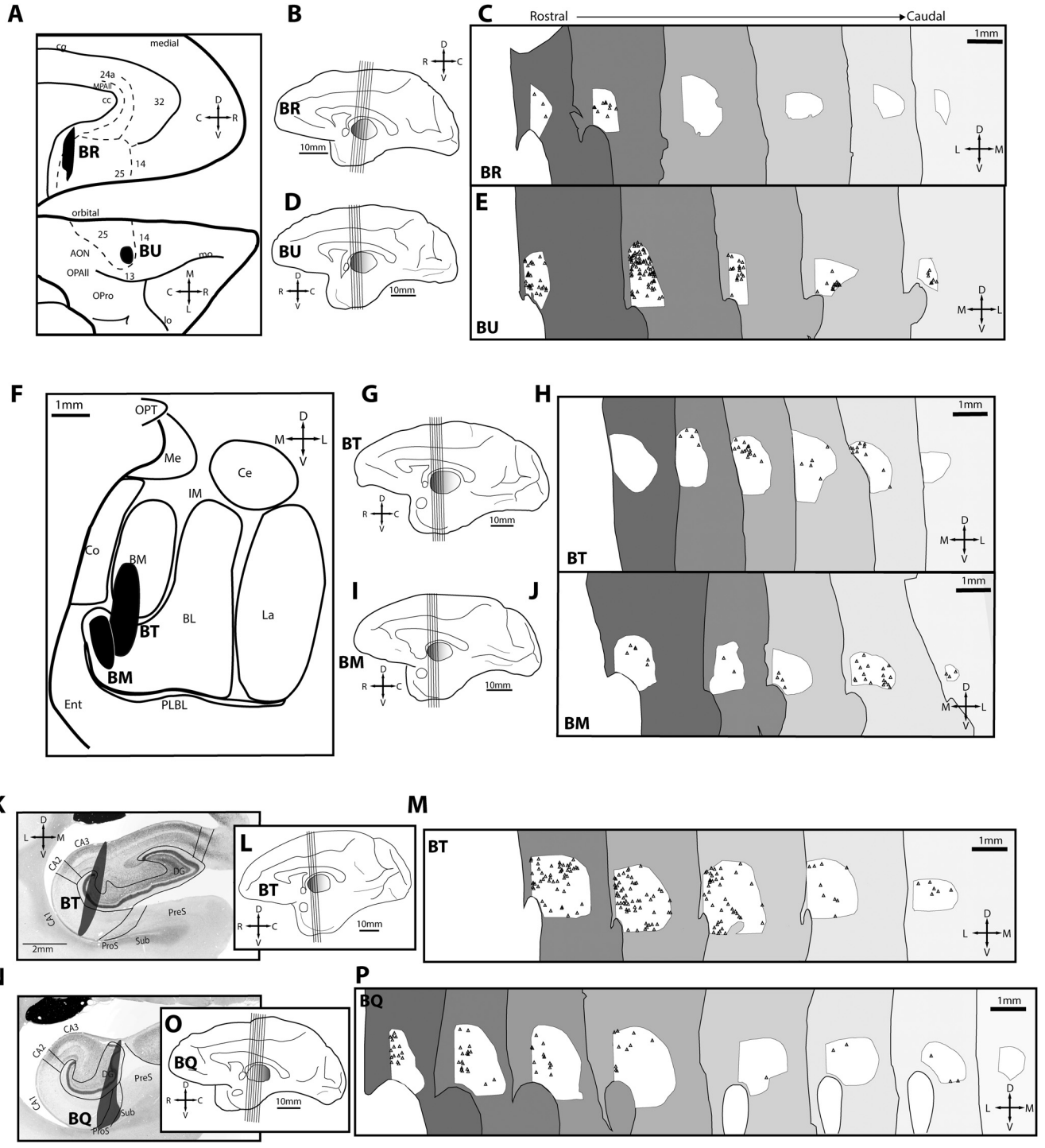

Figure 7. Maps of projection neurons in reuniens nucleus directed to A25, amygdala, and hippocampus. ***A***, Normalized A25 space depicts location of injection sites (black) in A25 that were used to map retrogradely labeled neurons in RE. BR featured a posterior medial injection site, whereas BU featured an anterior orbital injection site. Dashed lines depict areal boundaries. ***B***, Medial surface (case BR) with lines depicting planes of cut for sections sampled in ***C***. ***C***, Retrogradely labeled neurons in RE directed to medial A25 shown from rostral (left, dark gray) to caudal (right, light gray) levels (case BR). ***D–E***, Organization as above, but for tracer injection in orbital A25 (case BU). ***F***, Normalized amygdala space depicts location of injection sites (black) used to map retrogradely labeled neurons. One case (BT) featured an injection in the basomedial and ventral medial sector of the basolateral nucleus. The other case (BM) featured an injection in the ventral medial sector of the basolateral nucleus. ***G–H***, As above, but for case BT. ***I–J***, As above, but for another amygdalar case (case BM). ***K***, Injection site (black) in the hippocampus of case BT used to map retrogradely labeled neurons after tracer injection in CA3, DG, and CA1. ***L–M***, As above, but for hippocampal case BQ. ***N***, Injection site (black, case BQ) in used to map retrogradely labeled neurons in RE directed to hippocampus after tracer injection in CA1, DG, prosubiculum, and subiculum. ***O–P***, As above, but for case BQ with hippocampal injection as shown in ***N***. AON, Anterior olfactory nucleus; BL, basolateral nucleus of the amygdala; BM, basomedial nucleus of the amygdala; C, caudal; CA, cornu ammonis; Ce, central nucleus of the amygdala; cg, cingulate sulcus; Co, cortical nucleus of the amygdala; D, dorsal; DG, dentate gyrus; Ent, entorhinal cortex; III, third ventricle; IM, intercalated masses of the amygdala; L, lateral; La, lateral nucleus of the amygdala; lo, lateral orbital sulcus; M, medial; Me, medial nucleus of the amygdala; mo, medial orbital sulcus; MPAll, medial periallocortex; OPAll, orbital periallocortex; OPro, orbital proisocortex; OPT, optic tract; PLBL, paralaminar basolateral nucleus of the amygdala; ProS, prosubiculum; PreS, presubiculum; R, rostral; Sub, subiculum; V, ventral.

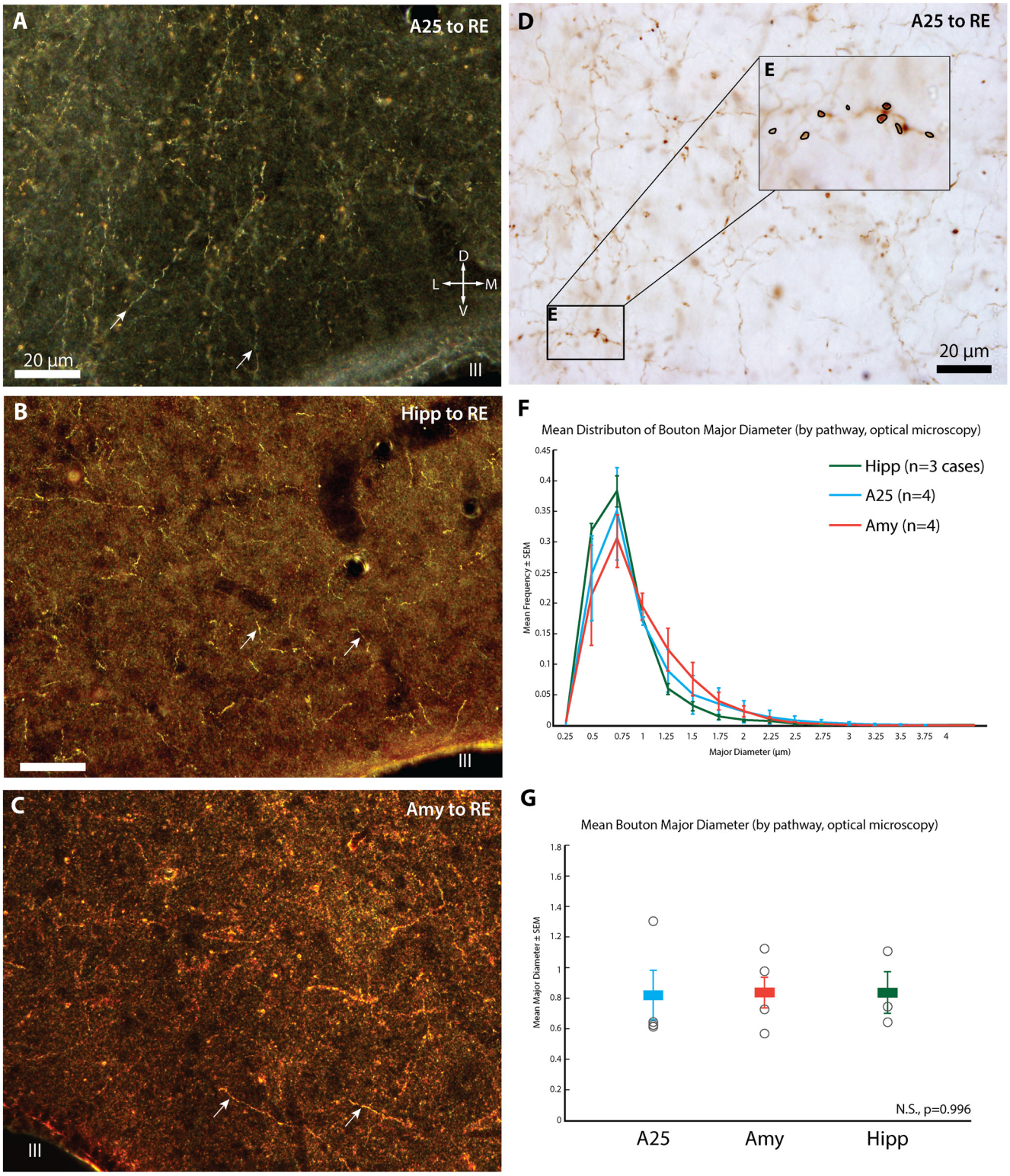

Figure 8. Bouton Diameters. ***A***, Darkfield photomicrograph of RE depicts axonal terminations (white arrows) from A25 (case BR, BDA tracer). Compass applies also to ***B, C***. ***B***, Darkfield photomicrograph of RE depicts axonal terminations (white arrows) from hippocampus (case BQ using Alexa488). ***C***, Darkfield photomicrograph of RE (white arrowhead, case BM, FR tracer) depicts axonal terminations (white arrows) from amygdala. ***D***, Brightfield photomicrograph of axonal terminations from A25 in RE (case BR, BDA tracer). ***E***, Inset, From ***D***. Axonal terminations in focus are circled to obtain their major diameter. ***F***, Histogram depicting distribution of mean bouton diameter per pathway. ***G***, Mean bouton diameter per pathway, color coded according to legend in ***F***. Open black circles indicate individual cases used for each pathway (A25, top to bottom: BR–BDA, *n*= 4870 boutons; BS–LY, *n* = 2271; BU–FE, *n* = 1969; BQ–FR, *n* = 1658; Amy, top to bottom: BD–BDA, *n* = 2029 boutons; BB–BDA, *n* = 1046; BM–FR, *n* = 2968; BT–CBL, *n* = 1341; Hipp, top to bottom: BS–CBL, *n* = 436; BT–FE, *n* = 1066; BQ–A488, *n* = 2507). Amy, Amygdala; BDA, biotinylated dextran amine; CBL, Cascade Blue; D, dorsal; FE, Fluoroemerald; FR, Fluororuby; Hipp, hippocampus; III, third ventricle; L, lateral; LY, Lucifer yellow; M, medial; N. S., not significant; V, ventral.

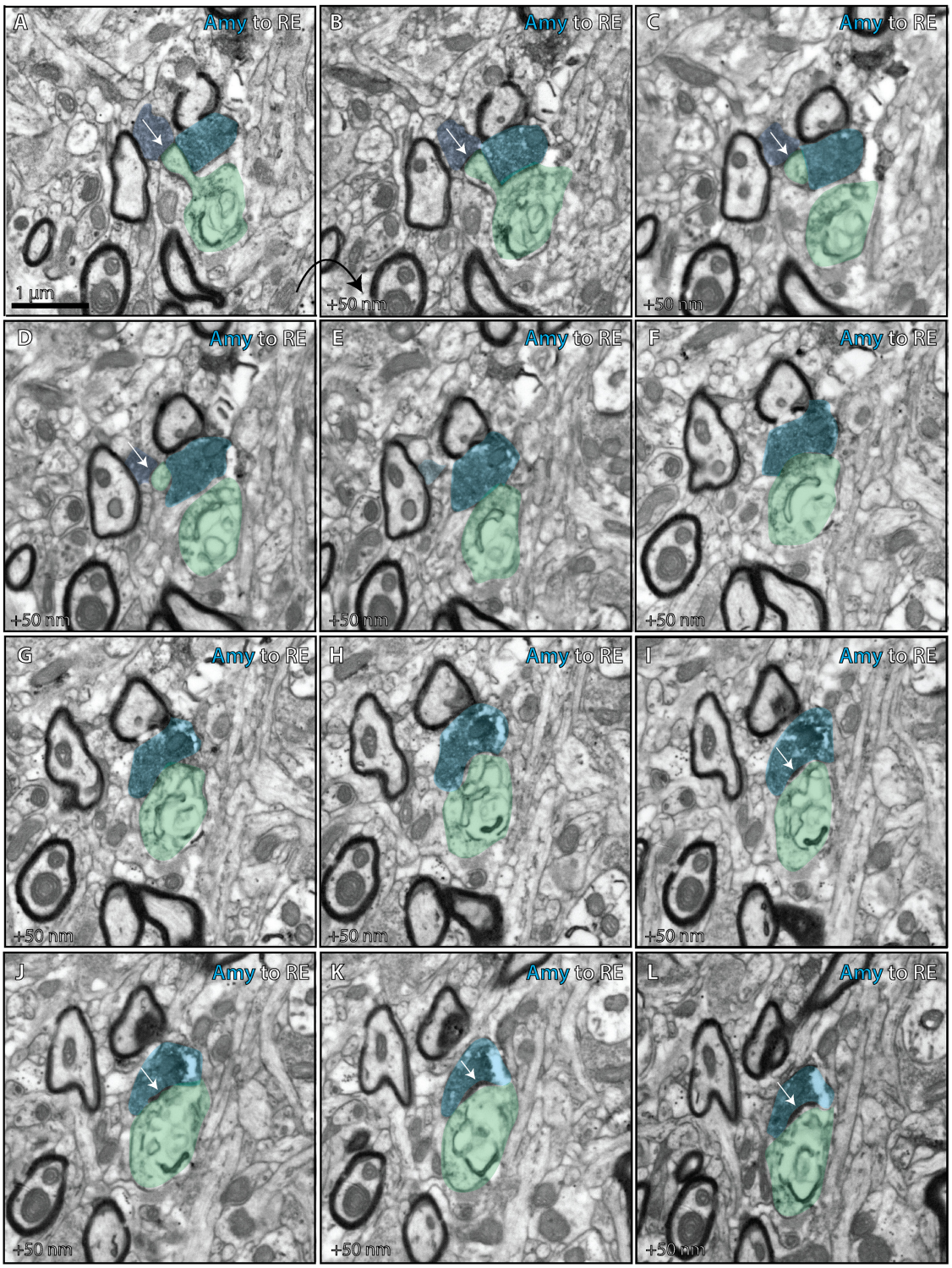

Figure 9. Ultrastructural analysis of amygdalar axon in the nucleus reuniens. Photomicrographs from serial EM depict ultrathin (50 nm) sections through the RE (case BQ, CBL tracer). Together they depict an amygdalar axon forming distinct terminations on a thorn and shaft of the same dendrite in RE. ***A–D***, One termination (dark blue) from the amygdalar axon forms an asymmetric synapse (white arrows) on a thorn of an RE dendrite (green). ***E–L***, A distinct termination from the same amygdalar axon (lighter blue) forms an asymmetric synapse (white arrows) on the shaft of the RE dendrite (green). Amy, Amygdala; CBL, Cascade Blue

inputs. In contrast, subcortical inputs to the PV core system originate in highly specific sensory and motor pathways, whereas inputs to the CB matrix system originate from widespread subcortical sources (Jones, 2009).

n intriguing aspect of matrix and core (excitatory) thalamocortical projections is their termination in cortical microenvironments dominated by inhibitory neurons labeled by the same calcium-binding proteins. For example, CB matrix thalamocortical neurons terminate mostly in superficial layers I–IIIa, where cortical CB inhibitory neurons are densest. Conversely, PV core thalamocortical neurons terminate in the middle layers (deep III to upper V), where cortical PV inhibitory neurons are densest.

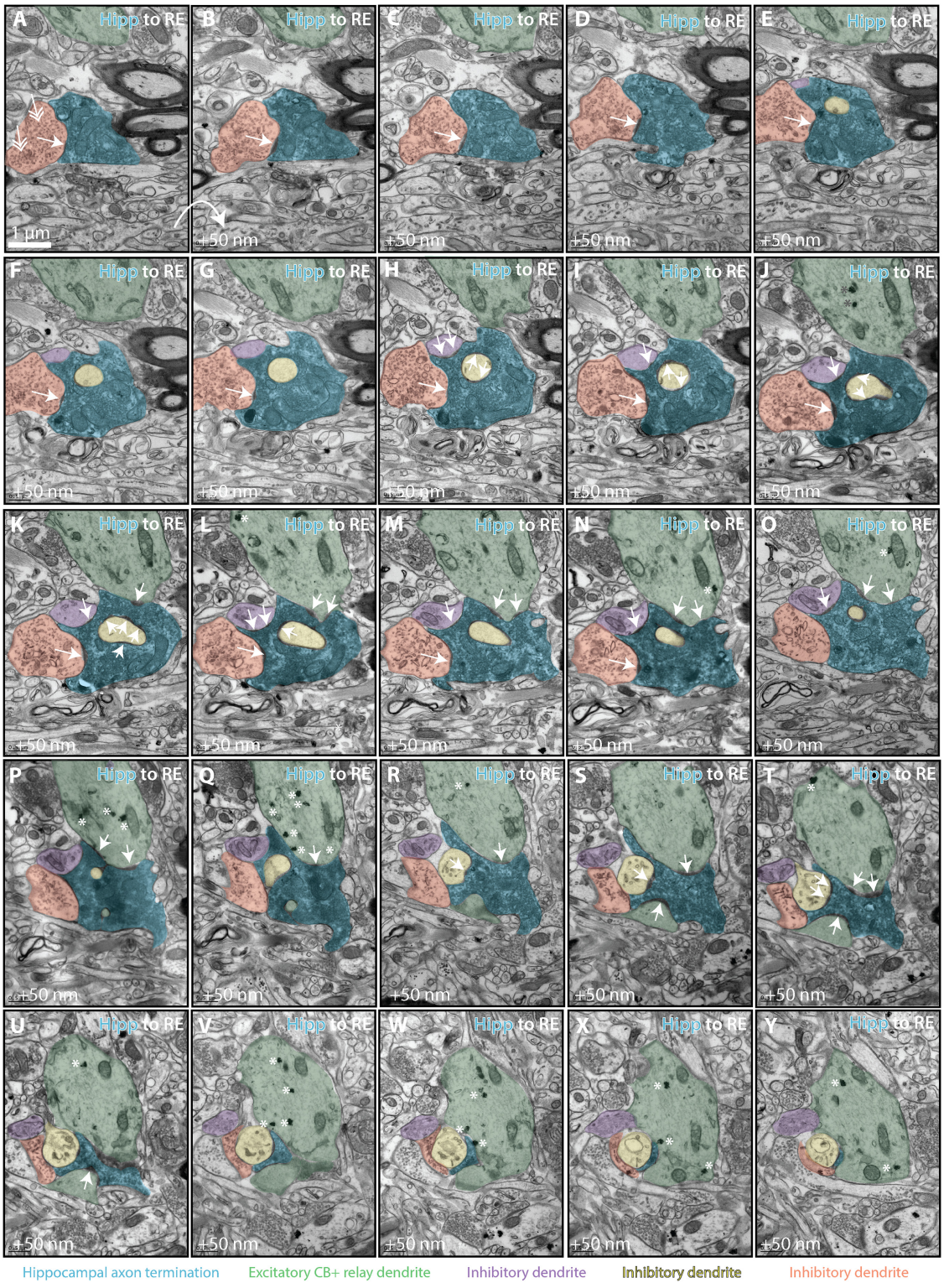

Figure 10. Ultrastructural analysis of multisynaptic hippocampal axon in the nucleus reuniens. Photomicrographs from serial EM depict ultrathin (50 nm) sections through RE (case BU, CBL tracer). Together they depict a hippocampal axon forming a multisynaptic complex with multiple dendrites in RE. ***A–G***, The hippocampal termination (blue) forms an asymmetric synapse (white arrow) with an inhibitory dendrite (pink), which contains pleomorphic vesicles (double-headed arrows in ***A***), presumed to emerge from a local inhibitory neuron. ***H–J***, The hippocampal termination forms asymmetric synapses (white arrows) with two new inhibitory dendrites (purple, yellow). ***K–R***, The hippocampal termination forms a perforated asymmetric synapse (white arrows) with the shaft of an excitatory dendrite (green) positive for CB (labeled with gold, which forms black clusters, asterisks). ***S–Y***, The hippocampal termination forms an asymmetric synapse (white arrows) with a thorn (green) from the CB-positive excitatory dendrite. CBL, Cascade Blue; Hipp, hippocampus.

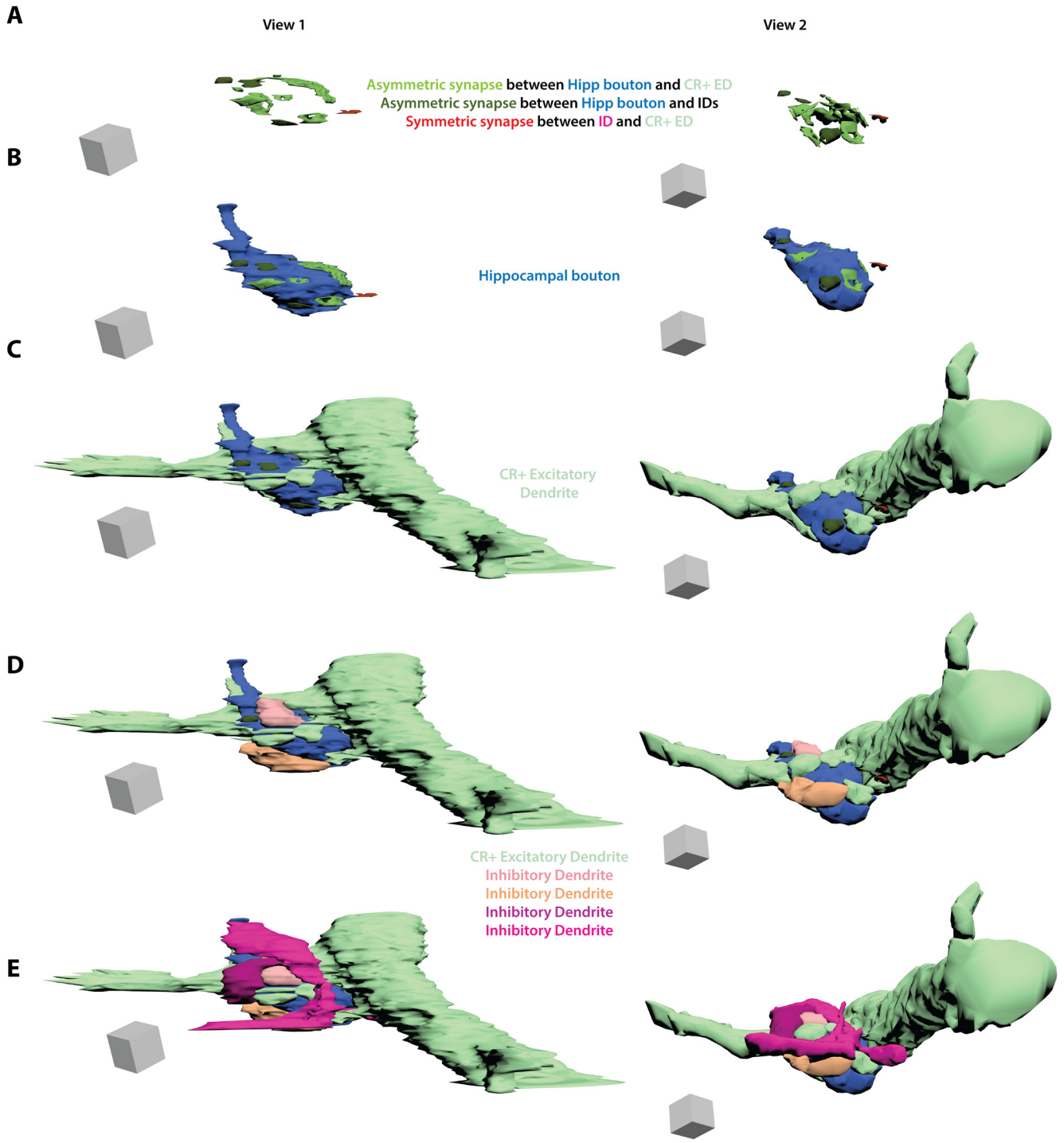

Figure 11. Three dimensional reconstruction of multisynaptic hippocampal termination in the nucleus reuniens. Three dimensional reconstruction from serial EM (case BQ, Alexa488 tracer). A hippocampal axon termination (blue) forms five distinct synapses with the shaft and thorns of a CR excitatory thalamic relay dendrite (CR+ ED, light green). The axon termination also forms four synapses with shafts of inhibitory dendrites (ID, orange or pink). One of these inhibitory dendrites also forms a synapse with the CR+ excitatory thalamic relay dendrite. ***A***, Asymmetric (excitatory, shades of green) synapses formed by hippocampal axon termination with thorns or shaft of CR+ ED or with IDs. Also shown is a symmetric (inhibitory) synapse (darker red) between one of the IDs and the CR+ ED. Scale box, 1 μm^3 ***B***, Same scenes with the addition of the hippocampal axon termination (blue). ***C***, Same scenes with the addition of the CR+ ED (light green). ***D***, Same scenes with the addition of two IDs (light pink and orange). ***E***, Same scenes with the addition of the remaining two IDs (darker pinks). Grey scale box, 1 μm^3. CBL, Cascade Blue; CR, calretinin; ED, excitatory relay dendrite; Hipp, hippocampus; ID, inhibitory dendrite.

Thalamic CR neurons, which are present in humans (Fortin et al., 1998; Munkle et al., 1999), have received scant study in non-human primates, with the exception of a small pathway from CR neurons in MDmc that projects to orbitofrontal cortex in rhesus monkeys (Timbie and Barbas, 2015). CR thalamocortical termination zones remain to be mapped in primates (Phillips et al., 2021), but their participation in matrix-dominant thalamic regions suggest a termination pattern in superficial layers, where numerous CR inhibitory neurons reside. In rats, RE axons terminate in the hippocampal stratum lacunosum-moleculare (Wouterlood et al., 1990; Vertes et al., 2006), where CR neurons predominate in primates (Wang and Barbas,

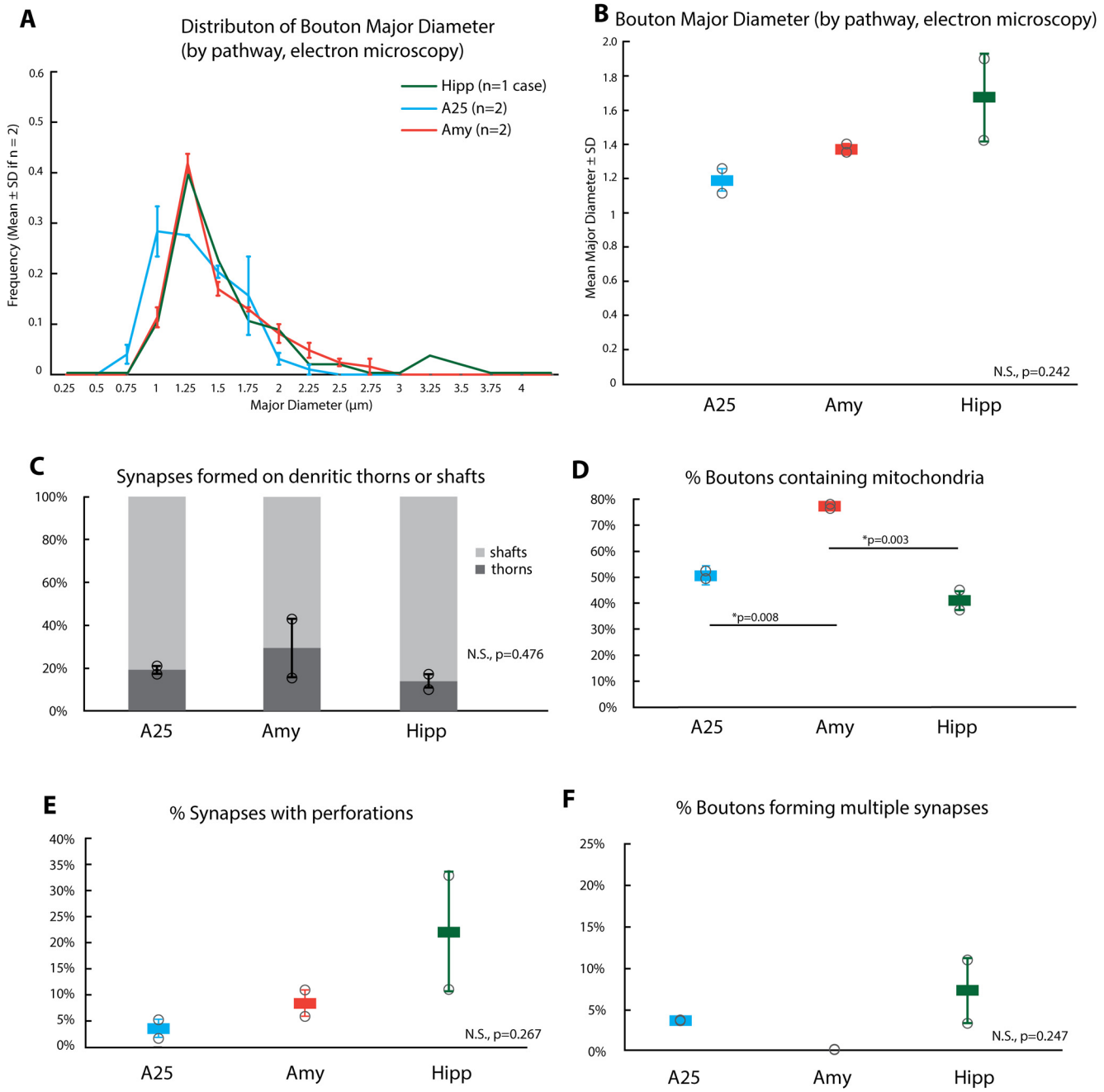

Figure 12. Quantitative ultrastructural features of pathways from hippocampus, A25, and amygdala to the nucleus reuniens. ***A***, Histogram depicts distribution of major diameter for hippocampus (case BQ, Alexa488), and mean distribution for A25 (BR, BDA tracer; BS, LY tracer) and amygdala (BW, FR tracer; BQ, CBL tracer) axonal terminations in RE from serial EM. ***B***, Major diameter by pathway as measured in photomicrographs from serial EM using color legend from ***A***. Open circles indicate individual case values (A25 top, BR, BDA tracer, $n = 47$ boutons; A25 bottom, BS, LY tracer, $n = 51$; Amy top, BW, FR tracer, $n = 32$; Amy bottom, BQ, CBL tracer, $n = 60$; Hipp top, BU, CBL tracer, $n = 7$; Hipp bottom, BQ, Alexa488 tracer, $n = 58$ with histogram in ***A***). ***C***, Percentage of synapses formed from A25, amygdala, and hippocampus terminations on dendritic thorns or shafts of postsynaptic targets in RE. Open circles indicate individual case values (A25 top, BR, BDA tracer, $n = 57$ synapses; A25 bottom, BS, LY tracer, $n = 52$; Amy top, BW, FR tracer, $n = 35$; Amy bottom, BQ, CBL tracer, $n = 64$; Hipp top, BU, CBL tracer, $n = 12$; Hipp bottom, BQ, Alexa488 tracer, $n = 66$). ***D***, Percentage of boutons that contained mitochondria per pathway. Open circles indicate individual case values (A25 top, BR, BDA tracer, $n = 55$ boutons; A25 bottom, BS, LY tracer, $n = 55$; Amy top, BQ, CBL tracer, $n = 35$; Amy bottom, BW, FR tracer, $n = 65$; Hipp top, BU, CBL tracer, $n = 9$; Hipp bottom, BQ, Alexa488 tracer, $n = 59$). ***E***, Percenaget of synapses formed by tracer-labeled axonal terminations per pathway in RE that were perforated. Open circles indicate individual case values (A25 top, BR, BDA tracer, $n = 58$ synapses; A25 bottom, BS, LY tracer, $n = 58$; Amy top, BQ, CBL tracer, $n = 64$; Amy bottom, BW, FR tracer, $n = 35$; Hipp top, BU, CBL tracer, $n = 12$; Hipp bottom, BQ, Alexa488 tracer, $n = 66$). ***F***, Percentage of tracer-labeled boutons per pathway that formed multiple synapses. Open circles indicate individual case values (A25, BR, BDA tracer, $n = 53$ synapses; BS, LY tracer, $n = 51$; Amy, BQ, CBL tracer, $n = 45$; BW, FR tracer, $n = 29$; Hipp top, BU, CBL tracer, $n = 9$; Hipp bottom, BQ, Alexa488 tracer, $n = 59$). Amy, Amygdala; CBL, Cascade Blue; FR, Fluororuby; hipp, hippocampus; LY, Lucifer yellow.

2018), a pattern akin to matrix thalamocortical projections to cortical layer I.

The calcium-binding proteins, which are expressed throughout the neuron, exquisitely control intracellular calcium homeostasis (Schwaller, 2010), and calcium is instrumental to dendritic activity and neuronal firing (Berridge, 1998; Arnsten et al., 2010; Larkum, 2013a; Arnsten et al., 2021). Alignment of cellwide calcium regulatory factors may facilitate entrainment between thalamocortical

projections and cortical inhibitory neurons to generate synchrony (Llinás et al., 1998; Hu and Agmon, 2016; Yu et al., 2019).

The predominance of matrix neurons in RE suggests mostly top-down interactions that impinge heavily on cortical layer I, like corticocortical feedback pathways. Layer I receives axons from long-range connections, apical dendrites from neurons below, and contains cell bodies of CR inhibitory neurons. The wide zones of feedback terminations from matrix-dominant thalamic nuclei may contribute to global integration and binding processes (Llinás et al., 1998; Jones, 2009; Larkum, 2013b; Redinbaugh et al., 2020). Specialized synaptic interactions between hippocampus and RE may lend context and temporality to these global integration processes, whereas connections between A25 and the amygdala with RE may contribute emotional valuation.

In conclusion, the primate RE has access to associative processes from mnemonic, cognitive, and emotional systems through bidirectional connections with hippocampus, A25, and the amygdala. Among these pathways, at least some hippocampal axons enter into synaptic triads with inhibitory neurons and local projection neurons in RE, whereas the amygdala has strong and widespread projections. The scatter of PV neurons suggests a small RE core system, whereas its bulk makeup of matrix projection neurons suggests a predominant upper-layer projection to mPFC. The similarities between the rodent and primate RE suggest common evolutionary advantages for adaptive behavior to seek rewards and avoid danger. The specializations in primates, however, may help explain the difficulty of translating complex conditions, such as mood disorders, and therapies from rodents to humans. These specialized features position the primate RE with its rich connections as a conduit for signal binding, conscious experience, and disorders thereof (Llinás et al., 1998; Van der Werf et al., 2002; Hannawi et al., 2015; Viena et al., 2021b).

References

Aggleton JP, Desimone R, Mishkin M (1986) The origin, course, and termination of the hippocampothalamic projections in the macaque. J Comp Neurol 243:409–421.

Alitto H, Rathbun DL, Vandeleest JJ, Alexander PC, Usrey WM (2019) The augmentation of retinogeniculate communication during thalamic burst mode. J Neurosci 39:5697–5710.

Amaral DG, Cowan WM (1980) Subcortical afferents to the hippocampal formation in the monkey. J Comp Neurol 189:573–591.

Arai R, Jacobowitz DM, Deura S (1994) Distribution of calretinin, calbindin-D28k, and parvalbumin in the rat thalamus. Brain Res Bull 33:595–614.

Arnsten AFT, Paspalas CD, Gamo NJ, Yang Y, Wang M (2010) Dynamic network connectivity: a new form of neuroplasticity. Trends Cogn Sci 14:365–375.

Arnsten AFT, Datta D, Wang M (2021) The genie in the bottle-magnified calcium signaling in dorsolateral prefrontal cortex. Mol Psychiatry 26:3684–3700.

Bachevalier J, Meunier M, Lu MX, Ungerleider LG (1997) Thalamic and temporal cortex input to medial prefrontal cortex in rhesus monkeys. Exp Brain Res 115:430–444.

Barbas H (1995) Anatomic basis of cognitive-emotional interactions in the primate prefrontal cortex. Neurosci Biobehav Rev 19:499–510.

Barbas H, Henion TH, Dermon CR (1991) Diverse thalamic projections to the prefrontal cortex in the rhesus monkey. J Comp Neurol 313:65–94.

Barbas H (2000a) Complementary role of prefrontal cortical regions in cognition, memory and emotion in primates. Adv Neurol 84:87–110.

Barbas H (2000b) Connections underlying the synthesis of cognition, memory, and emotion in primate prefrontal cortices. Brain Res Bull 52:319–330.

Berridge MJ (1998) Neuronal calcium signaling. Neuron 21:13–26.

Bokor H, Csaki A, Kocsis K, Kiss J (2002) Cellular architecture of the nucleus reuniens thalami and its putative aspartatergic/glutamatergic projection to the hippocampus and medial septum in the rat. Eur J Neurosci 16:1227–1239.

Cassel JC, Pereira de Vasconcelos A, Loureiro M, Cholvin T, Dalrymple-Alford JC, Vertes RP (2013) The reuniens and rhomboid nuclei: neuroanatomy, electrophysiological characteristics and behavioral implications. Prog Neurobiol 111:34–52.

Cassel JC, Ferraris M, Quilichini P, Cholvin T, Boch L, Stephan A, Pereira de Vasconcelos A (2021) The reuniens and rhomboid nuclei of the thalamus: a crossroads for cognition-relevant information processing? Neurosci Biobehav Rev 126:338–360.

Chiba T, Kayahara T, Nakano K (2001) Efferent projections of infralimbic and prelimbic areas of the medial prefrontal cortex in the Japanese monkey. Brain Res 888:83–101.

Cholvin T, Loureiro M, Cassel R, Cosquer B, Geiger K, De Sa Nogueira D, Raingard H, Robelin L, Kelche C, Pereira de Vasconcelos A, Cassel JC (2013) The ventral midline thalamus contributes to strategy shifting in a memory task requiring both prefrontal cortical and hippocampal functions. J Neurosci 33:8772–8783.

De Olmos J (1990) The human nervous system. San Diego: Academic.

Dermon CR, Barbas H (1994) Contralateral thalamic projections predominantly reach transitional cortices in the rhesus monkey. J Comp Neurol 344:508–531.

Devine MJ, Kittler JT (2018) Mitochondria at the neuronal presynapse in health and disease. Nat Rev Neurosci 19:63–80.

DeVito JL (1980) Subcortical projections to the hippocampal formation in squirrel monkey (*Saimira sciureus*). Brain Res Bull 5:285–289.

Dolleman-van der Weel MJ, Witter MP (2020) The thalamic midline nucleus reuniens: potential relevance for schizophrenia and epilepsy. Neurosci Biobehav Rev 119:422–439.

Dolleman-van der Weel MJ, Griffin AL, Ito HT, Shapiro ML, Witter MP, Vertes RP, Allen TA (2019) The nucleus reuniens of the thalamus sits at the nexus of a hippocampus and medial prefrontal cortex circuit enabling memory and behavior. Learn Mem 26:191–205.

Famiglietti EV, Jr. Peters A (1972) The synaptic glomerulus and the intrinsic neuron in the dorsal lateral geniculate nucleus of the cat. J Comp Neurol 144:285–334.

Ferraris M, Cassel JC, Pereira de Vasconcelos A, Stephan A, Quilichini PP (2021) The nucleus reuniens, a thalamic relay for cortico-hippocampal interaction in recent and remote memory consolidation. Neurosci Biobehav Rev 125:339–354.

Fiala JC (2005) Reconstruct: a free editor for serial section microscopy. J Microsc 218:52–61.

Fortin M, Asselin MC, Gould PV, Parent A (1998) Calretinin-immunoreactive neurons in the human thalamus. Neuroscience 84:537–548.

García-Cabezas MA, John YJ, Barbas H, Zikopoulos B (2016) Distinction of neurons, glia and endothelial cells in the cerebral cortex: an algorithm based on cytological features. Front Neuroanat 10:107.

Ghashghaei HT, Hilgetag CC, Barbas H (2007) Sequence of information processing for emotions based on the anatomic dialogue between prefrontal cortex and amygdala. Neuroimage 34:905–923.

Gundersen HJ (1986) Stereology of arbitrary particles. A review of unbiased number and size estimators and the presentation of some new ones, in memory of William R. Thompson. J Microsc 143:3–45.

Hannawi Y, Lindquist MA, Caffo BS, Sair HI, Stevens RD (2015) Resting brain activity in disorders of consciousness: a systematic review and meta-analysis. Neurology 84:1272–1280.

Hauer BE, Pagliardini S, Dickson CT (2019) The reuniens nucleus of the thalamus has an essential role in coordinating slow-wave activity between neocortex and hippocampus. eNeuro 6:ENEURO.0365-19.2019.

Herkenham M (1978) The connections of the nucleus reuniens thalami: evidence for a direct thalamo-hippocampal pathway in the rat. J Comp Neurol 177:589–610.

Hoistad M, Barbas H (2008) Sequence of information processing for emotions through pathways linking temporal and insular cortices with the amygdala. Neuroimage 40:1016–1033.
Hoover WB, Vertes RP (2007) Anatomical analysis of afferent projections to the medial prefrontal cortex in the rat. Brain Struct Funct 212:149–179.
Howard CV, Reed MG (1998) Unbiased stereology, three-dimensional measurement in microscopy. Oxford: BIOS Scientific.
Hsu DT, Price JL (2007) Midline and intralaminar thalamic connections with the orbital and medial prefrontal networks in macaque monkeys. J Comp Neurol 504:89–111.
Hu H, Agmon A (2016) Differential excitation of distally versus proximally targeting cortical interneurons by unitary thalamocortical bursts. J Neurosci 36:6906–6916.
Jayachandran M, Linley SB, Schlecht M, Mahler SV, Vertes RP, Allen TA (2019) Prefrontal pathways provide top-down control of memory for sequences of events. Cell Rep 28:640–654.e6.
John YJ, Bullock D, Zikopoulos B, Barbas H (2013) Anatomy and computational modeling of networks underlying cognitive-emotional interaction. Front Hum Neurosci 7:101.
John YJ, Zikopoulos B, Bullock D, Barbas H (2016) The emotional gatekeeper: a computational model of attentional selection and suppression through the pathway from the amygdala to the thalamic reticular nucleus. PLoS Comput Biol 12:e1004722.
Jones EG (1985) The thalamus. New York: Plenum.
Jones EG (1998a) A new view of specific and nonspecific thalamocortical connections. Adv Neurol 77:49–71.
Jones EG (1998b) Viewpoint: the core and matrix of thalamic organization. Neuroscience 85:331–345.
Jones EG (2001) The thalamic matrix and thalamocortical synchrony. Trends Neurosci 24:595–601.
Jones EG (2009) Synchrony in the interconnected circuitry of the thalamus and cerebral cortex. Ann N Y Acad Sci 1157:10–23.
Joyce MKP, Garcia-Cabezas MA, John YJ, Barbas H (2020) Serial prefrontal pathways are positioned to balance cognition and emotion in primates. J Neurosci 40:8306–8328.
Joyce MP, Barbas H (2018) Cortical connections position primate area 25 as a keystone for interoception, emotion, and memory. J Neurosci 38:1677–1698.
Kim U, McCormick DA (1998) The functional influence of burst and tonic firing mode on synaptic interactions in the thalamus. J Neurosci 18:9500–9516.
Lara-Vasquez A, Espinosa N, Duran E, Stockle M, Fuentealba P (2016) Midline thalamic neurons are differentially engaged during hippocampus network oscillations. Sci Rep 6:29807.
Larkum M (2013a) A cellular mechanism for cortical associations: an organizing principle for the cerebral cortex. Trends Neurosci 36:141–151.
Larkum ME (2013b) The yin and yang of cortical layer 1. Nat Neurosci 16:114–115.
Linley SB, Athanason AC, Rojas AKP, Vertes RP (2021) Role of the reuniens and rhomboid thalamic nuclei in anxiety-like avoidance behavior in the rat. Hippocampus 31:756–769.
Llinás R, Ribary U, Contreras D, Pedroarena C (1998) The neuronal basis for consciousness. Philos Trans R Soc Lond B Biol Sci 353:1841–1849.
Mathiasen ML, O'Mara SM, Aggleton JP (2020) The anterior thalamic nuclei and nucleus reuniens: so similar but so different. Neurosci Biobehav Rev 119:268–280.
McKenna JT, Vertes RP (2004) Afferent projections to nucleus reuniens of the thalamus. J Comp Neurol 480:115–142.
Medalla M, Lera P, Feinberg M, Barbas H (2007) Specificity in inhibitory systems associated with prefrontal pathways to temporal cortex in primates. Cereb Cortex 17 Suppl 1:i136–i150.
Munkle MC, Waldvogel HJ, Faull RL (1999) Calcium-binding protein immunoreactivity delineates the intralaminar nuclei of the thalamus in the human brain. Neuroscience 90:485–491.
Olszewski J (1952) The thalamus of the macaca mulatta. An atlas for use with the stereotaxic instrument. Basel: Karger.
Phillips JM, Kambi NA, Redinbaugh MJ, Mohanta S, Saalmann YB (2021) Disentangling the influences of multiple thalamic nuclei on prefrontal cortex and cognitive control. Neurosci Biobehav Rev 128:487–510.
Piantoni G, Halgren E, Cash SS (2016) The contribution of thalamocortical core and matrix pathways to sleep spindles. Neural Plast 2016:3024342.
Prasad JA, Macgregor EM, Chudasama Y (2013) Lesions of the thalamic reuniens cause impulsive but not compulsive responses. Brain Struct Funct 218:85–96.
Ramanathan KR, Maren S (2019) Nucleus reuniens mediates the extinction of contextual fear conditioning. Behav Brain Res 374:112114.
Ramanathan KR, Jin J, Giustino TF, Payne MR, Maren S (2018a) Prefrontal projections to the thalamic nucleus reuniens mediate fear extinction. Nat Commun 9:4527.
Ramanathan KR, Ressler RL, Jin J, Maren S (2018b) Nucleus reuniens is required for encoding and retrieving precise, hippocampal-dependent contextual fear memories in rats. J Neurosci 38:9925–9933.
Rasband WS (1997) ImageJ. Bethesda, MD: U.S.National Institutes of Health.
Redinbaugh MJ, Phillips JM, Kambi NA, Mohanta S, Andryk S, Dooley GL, Afrasiabi M, Raz A, Saalmann YB (2020) Thalamus modulates consciousness via layer-specific control of cortex. Neuron 106:66–75.e12.
Roberts AC, Tomic DL, Parkinson CH, Roeling TA, Cutter DJ, Robbins TW, Everitt BJ (2007) Forebrain connectivity of the prefrontal cortex in the marmoset monkey (*Callithrix jacchus*): an anterograde and retrograde tract-tracing study. J Comp Neurol 502:86–112.
Rollenhagen A, Lubke JH (2006) The morphology of excitatory central synapses: from structure to function. Cell Tissue Res 326:221–237.
Roy A, Svensson FP, Mazeh A, Kocsis B (2017) Prefrontal-hippocampal coupling by theta rhythm and by 2–5 Hz oscillation in the delta band: the role of the nucleus reuniens of the thalamus. Brain Struct Funct 222:2819–2830.
Saalmann YB (2014) Intralaminar and medial thalamic influence on cortical synchrony, information transmission and cognition. Front Syst Neurosci 8:83.
Scheel N, Wulff P, de Mooij-van Malsen JG (2020) Afferent connections of the thalamic nucleus reuniens in the mouse. J Comp Neurol 528:1189–1202.
Schwaller B (2010) Cytosolic Ca(2+) buffers. Cold Spring Harb Perspect Biol 2:a004051.
Sherman SM (2004) Interneurons and triadic circuitry of the thalamus. Trends Neurosci 27:670–675.
Sherman SM (2012) Thalamocortical interactions. Curr Opin Neurobiol 22:575–579.
Silva BA, Astori S, Burns AM, Heiser H, van den Heuvel L, Santoni G, Martinez-Reza MF, Sandi C, Gräff J (2021) A thalamo-amygdalar circuit underlying the extinction of remote fear memories. Nat Neurosci 24:964–974.
Stevens CF (2004) Presynaptic function. Curr Opin Neurobiol 14:341–345.
Timbie C, Barbas H (2014) Specialized pathways from the primate amygdala to posterior orbitofrontal cortex. J Neurosci 34:8106–8118.
Timbie C, Barbas H (2015) Pathways for emotions: specializations in the amygdalar, mediodorsal thalamic, and posterior orbitofrontal network. J Neurosci 35:11976–11987.
Timbie C, Garcia-Cabezas MA, Zikopoulos B, Barbas H (2020) Organization of primate amygdalar-thalamic pathways for emotions. PLoS Biol 18: e3000639.
Troyner F, Bertoglio LJ (2021) Nucleus reuniens of the thalamus controls fear memory reconsolidation. Neurobiol Learn Mem 177:107343.
Van der Werf YD, Witter MP, Groenewegen HJ (2002) The intralaminar and midline nuclei of the thalamus. Anatomical and functional evidence for participation in processes of arousal and awareness. Brain Res Brain Res Rev 39:107–140.
Varela C, Kumar S, Yang JY, Wilson MA (2014) Anatomical substrates for direct interactions between hippocampus, medial prefrontal cortex, and the thalamic nucleus reuniens. Brain Struct Funct 219:911–929.

Vertes RP, Hoover WB, Do Valle AC, Sherman A, Rodriguez JJ (2006) Efferent projections of reuniens and rhomboid nuclei of the thalamus in the rat. J Comp Neurol 499:768–796.

Vertes RP, Linley SB, Hoover WB (2015) Limbic circuitry of the midline thalamus. Neurosci Biobehav Rev 54:89–107.

Viena TD, Rasch GE, Silva D, Allen TA (2021a) Calretinin and calbindin architecture of the midline thalamus associated with prefrontal-hippocampal circuitry. Hippocampus 31:770–789.

Viena TD, Vertes RP, Linley SB (2021b) Discharge characteristics of neurons of nucleus reuniens across sleep-wake states in the behaving rat. Behav Brain Res 410:113325.

Vogt BA, Pandya DN, Rosene DL (1987) Cingulate cortex of the rhesus monkey: I. Cytoarchitecture and thalamic afferents. J Comp Neurol 262:256–270.

Wang J, Barbas H (2018) Specificity of primate amygdalar pathways to hippocampus. J Neurosci 38:10019–10041.

Wang J, John Y, Barbas H (2021) Pathways for contextual memory: the primate hippocampal pathway to anterior cingulate cortex. Cereb Cortex 31:1807–1826.

Wouterlood FG, Jorritsma-Byham B, Goede PH (1990) Combination of anterograde tracing with Phaseolus vulgaris-leucoagglutinin, retrograde fluorescent tracing and fixed-slice intracellular injection of Lucifer yellow. J Neurosci Methods 33:207–217.

Xu W, Sudhof TC (2013) A neural circuit for memory specificity and generalization. Science 339:1290–1295.

Yu J, Hu H, Agmon A, Svoboda K (2019) Recruitment of GABAergic interneurons in the barrel cortex during active tactile behavior. Neuron 104:412–427.e4.

Zikopoulos B, Barbas H (2007) Parallel driving and modulatory pathways link the prefrontal cortex and thalamus. PLoS One 2:e848.

Zikopoulos B, Barbas H (2012) Pathways for emotions and attention converge on the thalamic reticular nucleus in primates. J Neurosci 32:5338–5350.